III–V Based Magnetic Semiconductors

13

T. Jungwirth

Contents

Abstract

(Ga,Mn)As and related (III,Mn)V compounds are at the forefront of spintronics research exploring the synergy of ferromagnetism with the physics and the technology of semiconductors. Over the past 20 years, the research of (Ga,Mn)As has led to a deeper understanding of previously known spintronics phenomena,

T. Jungwirth (✉)
Institute of Physics ASCR, v.v.i., Praha 6, Czech Republic

School of Physics and Astronomy, University of Nottingham, Nottingham, UK
e-mail: jungw@fzu.cz

Y. Xu et al. (eds.), *Handbook of Spintronics*,
DOI 10.1007/978-94-007-6892-5_20

to discoveries of new effects, and to demonstrations of unprecedented functionalities of experimental spintronics devices with general applicability to a wide range of magnetic materials. In this chapter we review some of the basic structural, magnetic, electronic, and optical properties of the ferromagnetic (III,Mn)V semiconductors, as well as the devices fabricated from these model spintronics materials.

List of Acronyms

AMR	Anisotropic magnetoresistance
CB	Coulomb blockade
DOS	Density of states
DW	Domain wall
FMR	Ferromagnetic resonance
GGA	Generalized gradient approximations
GMR	Giant magnetoresistance
LSMR	Linear spin-Hall magnetoresistance
LT-MBE	Low-temperature molecular-beam epitaxy
MRAM	Magnetic random access memory
OSOT	Optical spin–orbit torque
OSTT	Optical spin–transfer torque
SET	Single-electron transistor
SHE	Spin-Hall effect
SOT	Spin–orbit torque
SQUID	Superconducting quantum interference device
STM	Scanning tunneling microscopy
STT	Spin–transfer torque
TAMR	Tunneling anisotropic magnetoresistance
TBA	Tight-binding approximation
TMR	Tunneling magnetoresistance
WB	Walker breakdown

Introduction

(Ga,Mn)As has been the most extensively studied member of the Mn-doped III–V family of magnetic semiconductors. It becomes ferromagnetic for doping above 1 % of the Mn local moments and acceptors. For semiconductor hosts this is a very high doping level which in case of (Ga,Mn)As and some related (III,Mn)V compounds can be achieved by the nonequilibrium, low-temperature molecular-beam-epitaxy (LT-MBE) technique [1–6].

Magnetic properties of the material can be modified by the means common in semiconductors, such as doping, electric fields, or light. For example, several experiments have verified that changes in the carrier density and distribution in thin (III,Mn)As films due to an applied gate voltage can induce reversible changes of the Curie temperature T_c, as illustrated in Fig. 1, and of other magnetic and

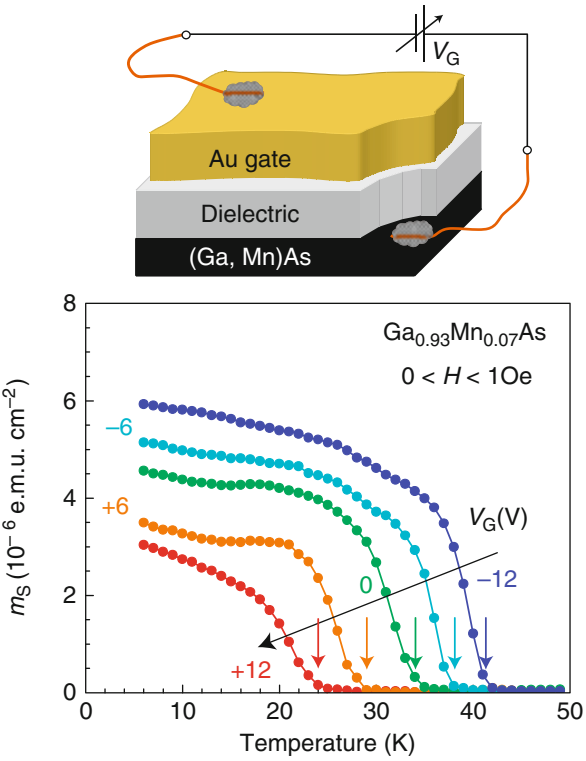

Fig. 1 *Top panel*: schematics of a field-effect transistor with an ultrathin (3.5 nm) (Ga,Mn)As layer. *Bottom panel*: experimental temperature dependence of the spontaneous moment for selected values of gate voltage. Temperatures at which moment disappears define the Curie temperature T_c, as marked by *arrows* (Reprinted by permission from Macmillan Publishers Ltd: Nature Physics [16], copyright (2009))

magneto-transport properties [7–16]. The interplay between optical and magnetic properties was demonstrated in experiments in which ferromagnetism in a (III,Mn)As system is turned on and off optically or in which recombination of spin-polarized carriers injected from the ferromagnetic semiconductor yields emission of circularly polarized light [17–19].

The tunability of magnetic properties and compatibility with established heterostructure growth and microfabrication techniques in semiconductors have made (Ga,Mn)As an ideal test-bed material for spintronics research. High-quality magnetic tunnel junctions have been demonstrated showing large tunneling magnetoresistances [20–23]. In the studies of spin–transfer torques in tunnel junctions [24] and domain walls [25–31], the dilute-moment p-type (Ga,Mn)As is unique for its low saturation magnetization and strong spin–orbit coupled valence band [32–34]. This implies low currents required to excite magnetization dynamics and the leading role of magnetocrystalline anisotropies over the dipolar shape anisotropy fields, which allows for unprecedented control of the magneto-transport phenomena ex situ by microfabrication [27, 35] or in situ by piezoelectric gating [31, 36–38].

Besides the more conventional spintronics effects such as the tunneling magnetoresistance and spin–transfer torque, (Ga,Mn)As studies have particularly important contributions to the research of spintronics phenomena based on the relativistic

spin–orbit coupling. Here among the new effects discovered in (Ga,Mn)As, and subsequently observed in other systems including conventional metal magnets, are the anisotropic magnetoresistance effects in nanostructures [39–44] and the current-induced spin–orbit torques observed in uniform magnetic structures [45, 46]. The optical activity of (Ga,Mn)As, characteristic of direct-gap semiconductors, has led to the discovery of the optical counterparts of the current-induced torques [47, 48].

In this chapter we provide an overview of the magnetic and electronic properties of (Ga,Mn)As and of the spintronics phenomena and devices that have been explored using this model material system. For more detailed discussions, we refer to other comprehensive review articles on ferromagnetic semiconductors [49–54].

Electronic Structure and Magnetic Coupling

The most stable position of Mn in the GaAs host lattice up to a certain level of Mn doping is on the Ga site. The isolated Mn_{Ga} substitutional impurity has the character of a local moment with zero orbital angular momentum and with spin $S = 5/2$ (Landé g-factor $g = 2$) due to the five $3d$ electrons and a moderately bound hole. The experimental acceptor binding energy of Mn_{Ga} is $E_a^0 \approx 0.1$ eV [55–59].

At concentrations $\ll 1$ % of Mn_{Ga}, (Ga,Mn)As is insulating and paramagnetic. Experimentally, ferromagnetism in (Ga,Mn)As is observed when Mn doping reaches approximately 1 %, and the system is still below but near the insulator-to-metal transition [60–63]. At these Min concentrations, the localization length of the holes is extended to a degree that allows them to mediate, via the $sp - d$ hybridization, ferromagnetic exchange interaction between Min local moments, even though the moments are dilute. Beyond 1.5 % Mn doping, (Ga,Mn)As becomes a degenerate semiconductor with a metallic-like conduction [49, 51, 63]. In the metallic regime, Mn provides delocalized holes with a density comparable to Mn density [64–66].

Unlike the metal–insulator phase transition, which is sharply defined in terms of the temperature $T = 0$ limit of the conductivity, the crossover in the character of states near the Fermi level in semiconductors with increased doping is gradual [51, 67–71]. At very weak doping, the Fermi level resides inside a narrow impurity band separated from the valence band by an energy gap of magnitude close to the impurity binding energy. At high doping when (Ga,Mn)As is ferromagnetic and metallic, the basic electronic structure and origin of magnetism have been a subject of some controversies. Here it is important to separate the physics and terminology sides of the debate.

We start with the character of the electronic structure. *Physics:* Based on a resonant tunneling study, it was concluded [72] that the effect of Mn impurities in ferromagnetic metallic (Ga,Mn)As is condensed within a narrow (~10's meV) detached impurity band, leaving the host GaAs valence band virtually unaffected. The photoemission studies [73, 74], on the other hand, showed that there is no gap between the Mn-induced impurity band and the GaAs valence bands and that Mn introduces changes throughout the entire valence band. Impurity and valence bands

are merged in ferromagnetic (Ga,Mn)As, according to photoemission. While in the resonant tunneling experiments the detached impurity band is not measured directly and its presence if inferred indirectly from electrical transport measurement through a heterostructure containing (Ga,Mn)As, the merged impurity and valence bands are observed directly in the photoemission spectroscopy of bare (Ga,Mn)As films. *Terminology:* For merged impurity and valence bands, assigning the Fermi level states to an impurity band or to a valence band if ambiguous and, therefore, only a matter of the choice of a preferred language.

A related but separate side of the debate concerns the nature of the magnetic coupling in the ferromagnetic metallic (Ga,Mn)As. *Physics:* Density functional theory calculations of the band structure of (Ga,Mn)As are in agreement with the photoemission measurements [73, 74]. Microscopic calculations of the (Ga,Mn)As band structure based on the multiorbital tight-binding-approximation (TBA) Anderson model [75], which are in broad agreement with the density functional theory, provide a direct link between microscopic electronic structure calculations and effective models of magnetic coupling mechanisms. In (Ga,Mn)As, a smaller part of the spectral weight near the Fermi energy is formed by Mn *d*-orbitals and a larger part by the host GaAs *sp*-orbitals [73–75], as shown in Fig. 2. The states near the Fermi energy are formed by *sp*-orbitals with moderately hybridized Mn *d* states. Zener's effective $sp - d$ kinetic-exchange model is derived by performing the Schrieffer–Wolff transformation of the $sp - d$ hybridization (and Coulomb interaction) into an effective exchange coupling between magnetic moments and carrier spins [51]. In the transformation, the $sp - d$ hybridization is treated perturbatively so the model accuracy increases with decreasing hybridization strength. For the moderate $sp - d$ hybridization in (Ga,Mn)As, one can expect sizable corrections beyond the weak $sp - d$ hybridization limit of the kinetic-exchange model. Simultaneously, the Fermi level states in (Ga,Mn)As are not characterized by occupying a narrow detached impurity band with a dominant Mn *d*-orbital composition. The material is, therefore, far from the corresponding Zener's $d - d$ hopping double-exchange model when viewed from the perspective of the orbital-resolved electronic structure.

The weak $sp - d$ hybridization kinetic-exchange model predicts a linear dependence of the mean-field Curie temperature T_c on the Mn moment density, and the $d - d$ hopping double-exchange model predicts a square-root dependence on the Mn moment density [52]. In both models the mean-field T_c increases monotonously with the Mn moment density, and calculations based on the density functional theory band structure show a sublinear dependence for (Ga,Mn)As [52]. Strongly distinct predictions of the two models are for the carrier-density dependence of the mean-field T_c. While the kinetic-exchange model predicts a weak monotonous increase of T_c with increasing density (to power 1/3 approximately), the double-exchange model predicts maximum T_c at half filling and zero T_c for zero carrier compensation (filled or empty $d - d$ hopping impurity band). Microscopic tight-binding Anderson [66] and density functional [52] calculations show initially an increasing T_c trend with increasing carrier density followed by a saturation near zero carrier compensation. The microscopic theories are consistent with

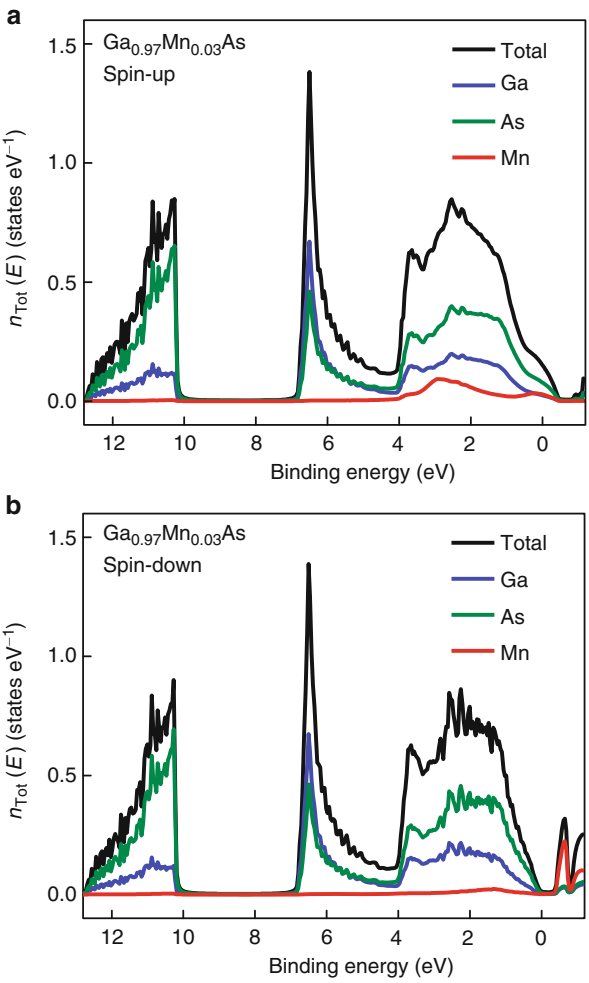

Fig. 2 (**a**) and (**b**) Calculated spin-resolved element and orbital-projected density of states (DOS) for $Ga_{0.97}Mn_{0.03}As$, with Ga, As, and Mn contributions indicated (Reprinted by permission from Macmillan Publishers Ltd: Nature Materials [73], copyright (2012))

experiments in Ref. [66] and [76]. On the other hand, the experimental work in Ref. [77] and [78] concluded that T_c collapses at zero carrier compensation. In Ref. [66] and [76], T_cs reach ~ 190 K while in Ref. [77] and [78] T_cs reach only ~ 90 K. Measurements in Ref. [66] and [76] were performed on (Ga,Mn)As materials prepared under carefully optimized synthesis conditions. The essential importance of optimized material synthesis for elucidating experimental doping trends in micromagnetic parameters of (Ga,Mn)As is thoroughly discussed in Ref. [79].

Terminology: It is only a matter of a preferred terminology how the mutually fully consistent physical results, as obtained among others in Refs. [52, 66, 73–76], are linked to Zener's magnetic exchange models. One may emphasize the presence of contributions beyond the weak hybridization limit in (Ga,Mn)As by using a term "moderate $sp-d$ hybridization kinetic exchange" [75], and others might prefer using a term "kinetic exchange with admixed double exchange" [52, 73].

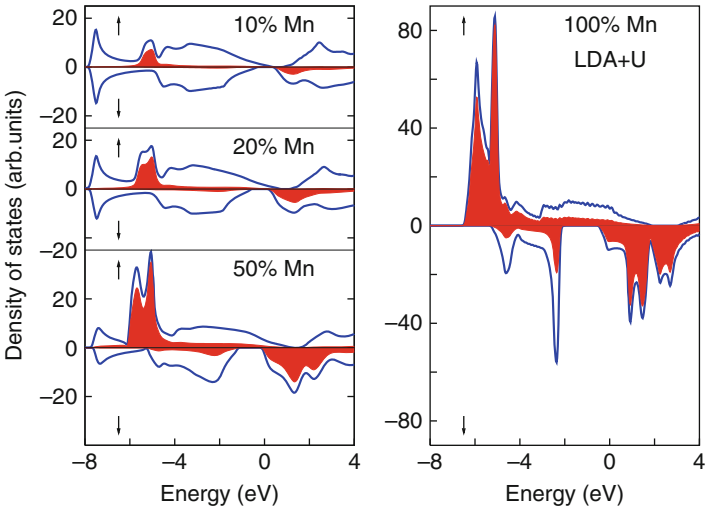

Fig. 3 DOS for (Ga,Mn)As mixed crystals with various contents of Mn obtained in the GGA + U theory. *Blue line* represents the total DOS while the red area shows the partial density of Mn *d* states (From Ref. [75]. Reprinted with permission from J. Mašek et al., Physical Review Letters, 105, 2010. Copyright (2010) by the American Physical Society)

In Fig. 3 we show density of states (DOS) over the entire Mn_{Ga} doping range obtained from the generalized gradient approximation (GGA) + U density functional calculations [52, 75]. The GGA + U, the TBA-Anderson, and the kinetic-exchange Zener theories all provide a consistent picture of the band structure of ferromagnetic (Ga,Mn)As. Simultaneously, it is important to keep in mind that the moderate acceptor binding energy of Mn_{Ga} shifts the insulator-to-metal transition to orders of magnitude higher doping densities than in the case of common shallow nonmagnetic acceptors, as mentioned above [63, 75]. Disorder and correlation effect, therefore, play a comparatively more significant role in (Ga,Mn)As than in degenerate semiconductors with common shallow dopants, and any simplified one-particle band picture of ferromagnetic (Ga,Mn)As can only represent a proxy to the electronic structure of the material.

To illustrate the role of strong intrinsic disorder in ferromagnetic (Ga,Mn)As, we show in Fig. 4 the local DOS along one of the directions inside the simulation cells illustrated in Fig. 5 for 5 % Mn doping. In the model, the band structure and disorder effects are treated at an equal level by using exact diagonalization supercell simulation method [80]. There is an extensive weight of the density of states in the mid-gap region which arises from the deep bonding states created by neighboring Mn impurities. The higher energy tail of the disordered valance band comprises localized states as highlighted in Fig. 4b. On the other hand, the Fermi energy is located deep in the delocalized region away from the mobility edge. The spatial inhomogeneity of the distribution of states in the gap region and the peaks formed by bonding states in the gap region are consistent with scanning tunneling

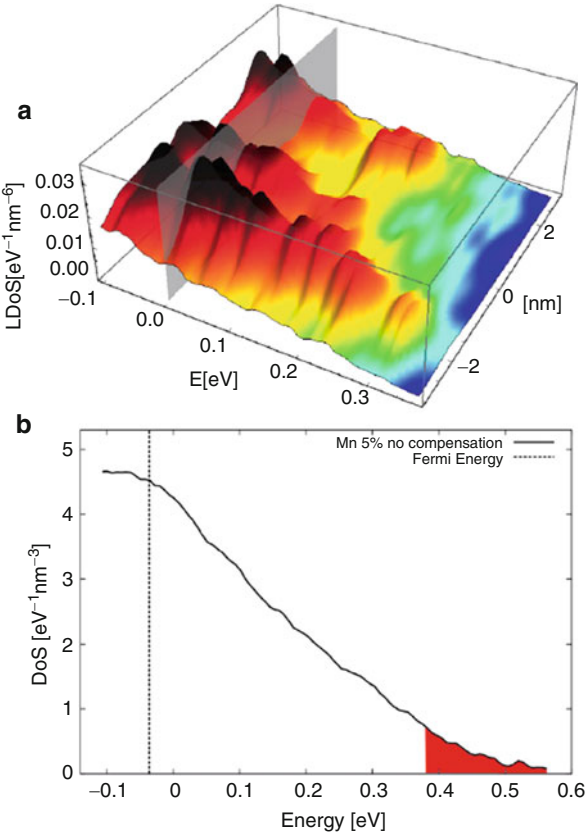

Fig. 4 (**a**) Local DOS for 5 % Mn doping. The *plot* shows different positions along the x-axis of the simulation supercell which is shown in Fig. 5. The *vertical plane* shows the position of the Fermi energy. The results are from the theoretical Ref. [80] and agree qualitatively with the STM experiments in Ref. [81]. (**b**) DOS for 5 % Mn doping. *Red area* shows the localized states

microscopy (STM) experiments [81]. The effect of strong disorder on the wave functions is illustrated in Fig. 5 which compares the probability distributions of a localized state near the disordered valance band edge, a delocalized state near the Fermi energy, and a state near the mobility edge.

Curie Temperature and Doping Trends

As seen in Fig. 3, the bands evolve continuously from the intrinsic nonmagnetic semiconductor GaAs, via the degenerate ferromagnetic semiconductor (Ga,Mn)As to the ferromagnetic metal MnAs. From this it can be expected that T_c of MnAs, with the value close to room temperature (350 K for cubic MnAs inclusions in (Ga, Mn)As [82, 83]), sets the upper theoretical bound of achievable T_cs in (Ga,Mn)As across the entire doping range. In experiment, the Mn_{Ga} doping is limited to approximately 10 % with corresponding T_c reaching 190 K in uniform thin-film crystals prepared by optimized LT-MBE synthesis and post-growth annealing. In these samples the hole density is in the $\sim 10^{20} - 10^{21}$ cm^{-3} range, i.e., several

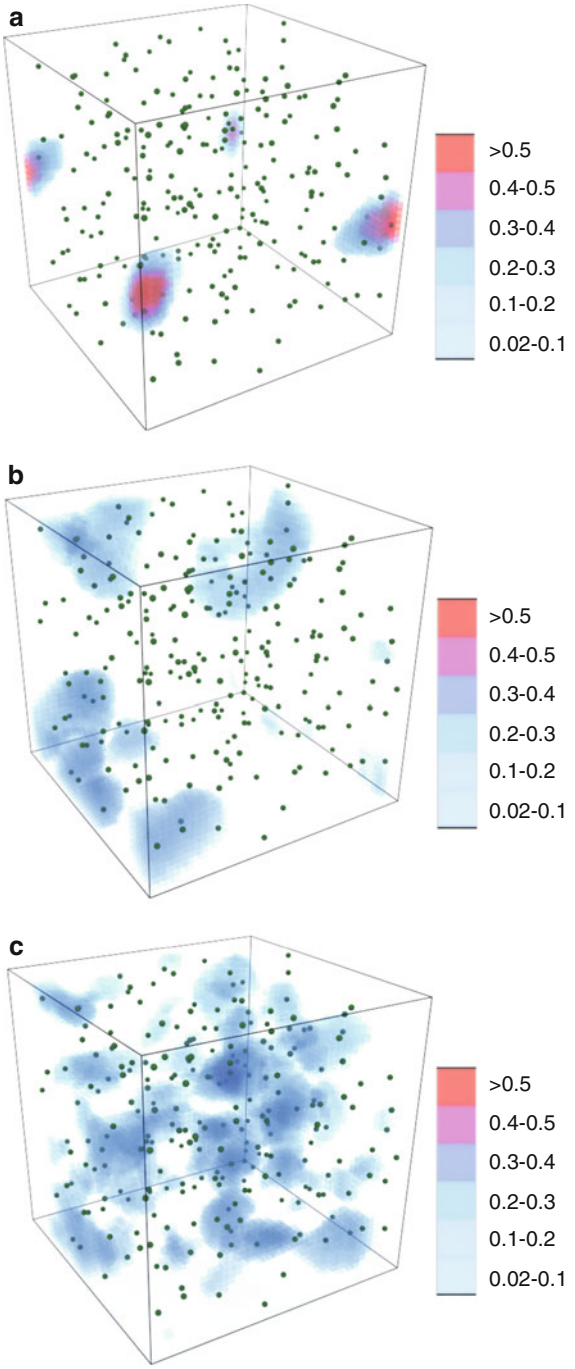

Fig. 5 Wave function probability distribution of a localized state near the disordered valance band edge (**a**), a delocalized state near the Fermi energy (**c**), and a state near the mobility edge (**b**) (From Ref. [80]. Reprinted with permission from Huawei Gao et al., Physical Review B, 91, 2015. Copyright (2015) by the American Physical Society)

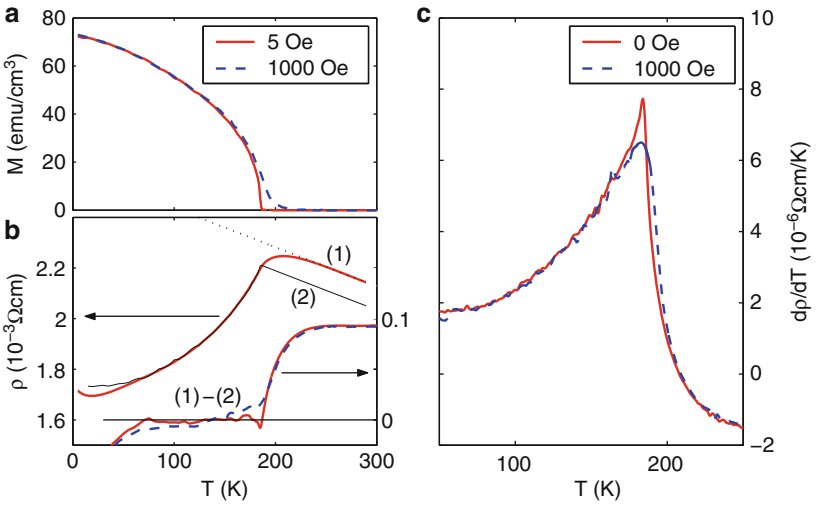

Fig. 6 (**a**) Temperature-dependent SQUID magnetization of an optimized 12.5 % Mn-doped (Ga, Mn)As measured at 5 and 1000 Oe. (**b**) Measured resistivity $\rho(T)$ at zero field (1), the fit of $\rho(T)$ by $\rho_{fit}(T) = c_0 + c_{nm}T + c_{m2}M^2(T) + c_{m4}M^4(T)$ (2), and the difference $\rho(T) - \rho_{fit}(T)$ for the 5 and 1000 Oe field measurements (*right-hand scale*). (**c**) Temperature derivative of the measured resistivity at 5 and 1000 Oe. The peak in zero-field $d\rho/dt$ coincides, within the experimental error, with the SQUID $T_c = 185$ K (From Ref. [84], Reprinted with permission from V. Novák et al., Physical Review Letters, 101, 2008. Copyright (2008) by the American Physical Society)

orders of magnitude higher than densities in commonly used nonmagnetic semiconductors but also one to two orders of magnitude lower than is typical for metals.

A detailed measurement of the Curie temperature in a high-quality (Ga,Mn)As material is illustrated in Fig. 6 [84]. Figure 6a shows magnetization $M(T)$ measured along the easy axis in this material over the whole studied temperature range. The remanence vanishes sharply at $T \to T_c^-$. Figure 6b shows results of corresponding measurements of the resistivity $\rho(T)$. A useful insight into the physics of the shoulder in $\rho(T)$ near T_c is obtained by first removing the nonmagnetic part in the temperature dependence, $c_{nm}T$, which is approximated by linearly extrapolating from the high-temperature $\rho(T)$ data (see the straight dotted line in Fig. 6b). The measured $M(T)$ then allows to subtract the contribution from uncorrelated scattering, assuming a M^2 expansion dependence [5, 85–87]. On the ferromagnetic side, a very close fitting is achieved by $\rho_{fit}(T) = c_0 + c_{nm}T + c_{m2}M^2(T) + c_{m4}M^4(T)$. On the paramagnetic side, the nose dive of the remaining magnetic contribution to $\rho(T)$ suggests that the shoulder in the measured resistivity originates from a singular behavior at $T \to T_c^+$ rather than from disorder broadening effects. The singularity is revealed by numerically differentiating the experimental zero-field $\rho(T)$ curve, as shown in Fig. 6c. The position of the sharp peak in $d\rho/dT$ coincides with the Curie temperature determined from $M(T)$.

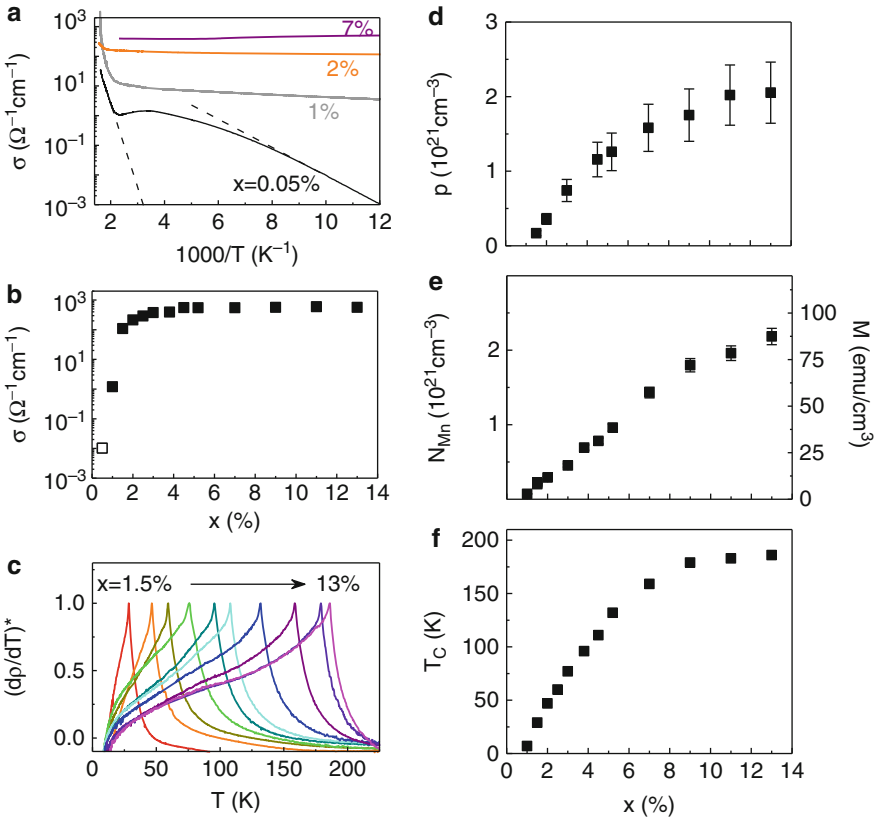

Fig. 7 (**a**) Temperature dependence of the conductivity $\sigma(T)$ of optimized (Ga,Mn)As epilayers with depicted nominal Mn doping. *Dashed lines* indicate the activated parts of $\sigma(T)$ of the insulating paramagnetic (Ga,Mn)As with 0.05 % Mn doping, corresponding to the Mn acceptor level and the band gap, respectively. (**b**) Conductivity at 4 K as a function of the nominal Mn doping. Open symbol corresponds to a paramagnetic sample. (**c**) Sharp Curie point singularities in the temperature derivative of the resistivity in the series of optimized ferromagnetic (Ga,Mn)As epilayers with metallic conduction. (**d–f**) Hole density p, magnetization M and corresponding Mn moment density N_{Mn}, and Curie temperature T_c as a function of the nominal Mn doping in the series of optimized (Ga,Mn)As epilayers (From Ref. [79]. Copyright © 2013, Rights Managed by Nature Publishing Group)

The $d\rho/dT$ singularity described in Fig. 6 is a generic characteristic of optimized (Ga,Mn)As films spanning a wide range of Mn dopings. This is illustrated in Fig. 7c together with the other doping characteristics of the optimized materials shown in Fig. 7. From the doping trends seen in Fig. 7, the uniform (Ga,Mn)As materials with minimized extrinsic disorder can be divided into the following groups: At nominal dopings below ~ 0.1 %, the (Ga,Mn)As materials are paramagnetic, strongly insulating, showing signatures of the activated transport corresponding to valence

band−impurity band transitions at intermediate temperatures and valence band−conduction band transitions at high temperatures (see Fig. 7a) [63, 79]. For higher nominal dopings, $0.5 \lesssim x \lesssim 1.5$ %, no clear signatures of activation from the valence band to the impurity band are seen in the dc transport, indicating that the bands start to overlap and mix, yet the materials remain insulating. At $x \approx 1.5$ %, the low-temperature conductivity of the film increases abruptly by several orders of magnitude (see Fig. 7b), and the system turns into a degenerate semiconductor. The onset of ferromagnetism occurs already on the insulating side of the transition at $x \approx 1$ %. All ferromagnetic samples over a broad nominal Mn-doping range can have sharp Curie point singularities when synthesized under individually optimized growth and post-growth annealing conditions (see Fig. 7c).

The hole concentration p can be measured by the slope of the Hall curve at high fields with an error bar due to the multi-band nature estimated to ~ 20 % [66]. Within this uncertainty, the overall trend shows increasing p with increasing doping in the optimized materials, as shown in Fig. 7d. Similarly, the saturation moment and T_c steadily increase with increasing nominal doping up to $x \approx 13$ %, as shown in Fig. 7e, f. Assuming 4.5 μ_B per Mn atom [88], the density N_{Mn} of uncompensated Mn_{Ga} moments can be inferred from the magnetization data (see left y-axis in Fig. 7e). Since there is no apparent deficit of p compared to N_{Mn} and since the interstitial Mn impurity [89–91] compensates one local moment but two holes, it can be concluded that interstitial Mn, which is the key contributor to extrinsic disorder, is removed in the optimally grown and annealed epilayers. Hence, a broad series of optimized (Ga,Mn)As materials can be prepared with reproducible characteristics, showing an overall trend of increasing saturation moment with increasing x, increasing T_c (reaching ~ 190 K), and increasing hole density. The materials have no measurable charge or moment compensation of the substitutional Mn_{Ga} impurities and have a large degree of uniformity.

Magnetic Anisotropy Effects in Films and Devices

Micromagnetic Parameters

The magnetic anisotropy relates to the dependence of the total energy of the magnetic material on the direction of the magnetization vector. In magnetic memories it is the key parameter that determines the retention of the stored information. In the optimized (Ga,Mn)As epilayers grown on GaAs, the internal magnetic anisotropy fields are dominated by three components. The out-of-plane component K_{out} is a sum of the thin-film shape anisotropy and the relativistic magnetocrystalline anisotropy due to the compressive growth strain in (Ga,Mn)As deposited on the GaAs substrate. The cubic magnetocrystalline anisotropy K_c reflects the zinc-blended crystal structure of the host semiconductor. The additional uniaxial anisotropy component K_u along the in-plane diagonal is not associated with any measurable macroscopic strain in the epilayer, and its origin is still debated.

In a ferromagnetic resonance experiment, the precession frequency is given by

$$f = \frac{g\mu_B}{h}\left[H_{ext}\cos(\varphi-\varphi_H) - 2K_{out} + K_c(3+\cos 4\varphi)/2 + 2K_u \sin^2(\varphi-\pi/4) + \Delta H_n\right]^{1/2} \times \left[H_{ext}\cos(\varphi-\varphi_H) + 2K_c\cos 4\varphi - 2K_u \sin 2\varphi + \Delta H_n\right]^{1/2}, \quad (1)$$

where g is the Landé g-factor of Mn moments, μ_B is the Bohr magneton, φ and φ_H are the in-plane magnetization and external magnetic-field angles measured from the [100] crystal axis, and ΔH_n is the shift of the resonant field for the higher-index n spin wave modes with respect to the $n = 0$ uniform precession mode. In order to uniquely determine the anisotropy constants, field-dependent precession frequency measurements were performed on the optimized films by a magneto-optical pump-and-probe technique and complemented by the superconducting quantum interference device (SQUID) measurements [79].

The values of K_{out} and K_c for the given Mn doping are well reproducible in materials whose synthesis yields the same optimized values of the basic structural, magnetic, and transport properties. For the K_u constant, variations in the width of the optimized thin (Ga,Mn)As films or of other otherwise insignificant changes of the growth or annealing conditions may yield sizable changes of K_u. This indicates a more subtle, extrinsic nature of this magnetic anisotropy component.

The sign of K_{out} implies that the (Ga,Mn)As/GaAs materials are in-plane ferromagnets. The competing magnitudes of K_c and K_u and the different doping trends of these two in-plane magnetic anisotropy constants (see Fig. 8a) are therefore crucial for the micromagnetics of the materials. The biaxial anisotropy K_c dominates at very low dopings, and the easy axis aligns with the main crystal

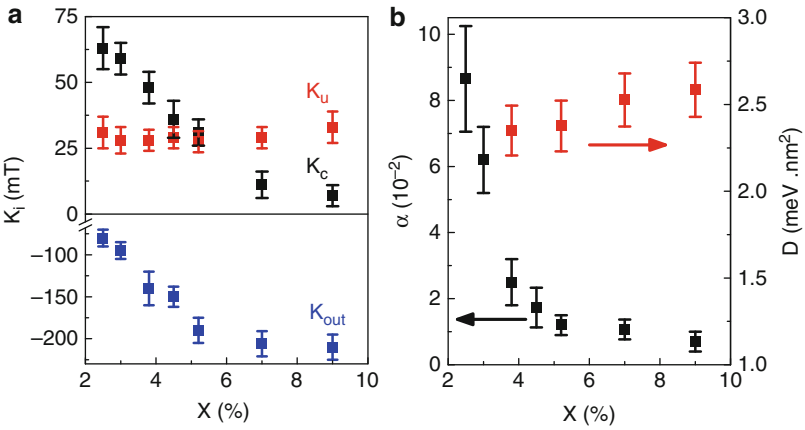

Fig. 8 (**a**) Dependence of magnetic anisotropy constants on nominal Mn doping. (**b**) Dependence of the Gilbert damping constant α and the spin stiffness constant D on nominal Mn doping. Measurements were performed at 15 K (From Ref. [79]. Copyright © 2013, Rights Managed by Nature Publishing Group)

axis [100] or [010]. At intermediate dopings, the uniaxial anisotropy K_u is still weaker but comparable in magnitude to K_c. In these samples the two equilibrium easy axes are tilted toward the $[1\bar{1}0]$ direction, and their angle is sensitive to small changes of temperature or externally applied electrostatic or piezo voltages [7, 8, 11–14, 31, 36–38].

The origin of the magnetocrystalline anisotropies is in the spin–orbit coupling of the valence band holes mediating the ferromagnetic Mn–Mn coupling, as described on a qualitative or semiquantitative level by the model, kinetic-exchange Hamiltonian theory [92–94].

For completeness we show in Fig. 8b the Gilbert damping constants and spin stiffnesses inferred from the same set of measurements as for the magnetic anisotropy constants. Their values are also consistent with theory predictions for the spin–orbit coupled disordered valence band of (Ga,Mn)As [32, 95–98].

Resistors

Resistors, capacitors, and transistors are among the key elements of electronic circuits. Here and in sections "Tunnel Junctions," "Capacitors," and "Transistors," we review how research in (Ga,Mn)As has contributed to studies of the relativistic magnetic anisotropy phenomena reflected in functionalities of these electronic devices.

In general, magnetic effects on transport properties of conductors can be ascribed to three different categories: ordinary (orbital), due to the Lorentz force; spin-dependent, due to spin splitting of bands through ferromagnetism or the Zeeman effect; and extraordinary, relativistic in origin through the spin–orbit interaction. Well-known examples of these effects are Lorentz magnetoresistance, giant magnetoresistance (GMR) [99], and anisotropic magnetoresistance (AMR) [100], respectively. (Ga,Mn)As represents a favorable model system for understanding the phenomenology and detailed microscopic origin of the AMR in ohmic resistors [101–108].

AMR is the symmetric magnetoresistance coefficient with the longitudinal and transverse resistivities obeying, $\rho_L(\mathbf{M}) = \rho_L(-\mathbf{M})$ and $\rho_T(\mathbf{M}) = \rho_T(-\mathbf{M})$, where $\mathbf{M}$ has an arbitrary orientation. AMR was discovered by Lord Kelvin in transition metal ferromagnets [109] and was used in the first generation of hard drive read heads and magnetoresistive random access memories (MRAMs) [110].

Among the remarkable AMR features of (Ga,Mn)As ferromagnetic semiconductors are the opposite sign of the noncrystalline component, compared to most metal ferromagnets, and the crystalline terms reflecting the rich magnetocrystalline anisotropies [101–107]. In Fig. 9 we show an example of AMR data replotted from Ref. [107] which reports a systematic experimental and phenomenological study of the AMR coefficients in (Ga,Mn)As films, grown on (001)- and (113)A-oriented GaAs substrates.

Microscopic numerical simulations [102, 111] consistently describe the sign and magnitudes of the noncrystalline AMR in the standard (Ga,Mn)As materials with

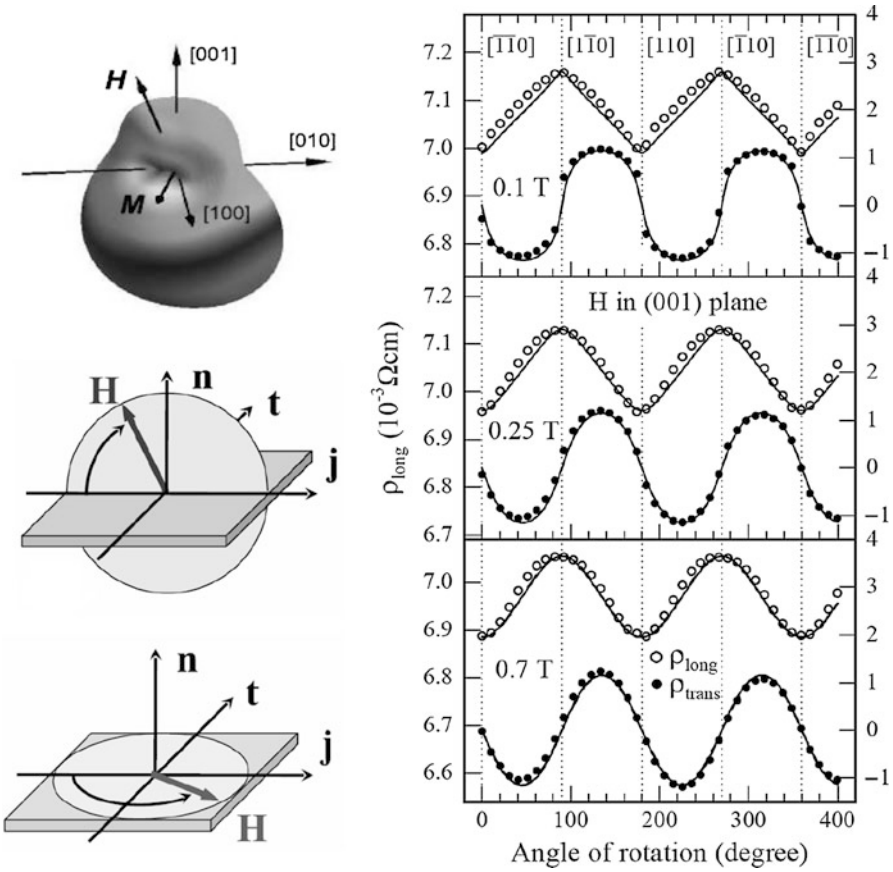

Fig. 9 *Left panels*: magnetization and external magnetic-field vectors with different orientations below saturation fields. The out-of-plane and in-plane AMR measurement geometries. *Right panel*: measured longitudinal and transverse in-plane AMR curves at external fields smaller than the saturation field (0.1 and 0.25 T) and larger than the saturation field (0.7 T). The *solid lines* represent fits to the experimental data (From Ref. [107]. Reprinted with permission from W. Limmer et al., Physical Review B, 74, 2006. Copyright (2006) by the American Physical Society)

metallic conductivities and capture the presence of the more subtle crystalline terms associated with, e.g., growth-induced strain [104, 111]. In the following paragraphs, we describe some of the rich AMR phenomenology in (Ga,Mn)As in more detail and explain the basic microscopic physics of the AMR in dilute-moment ferromagnets. For simplicity we discuss only AMR in saturating magnetic fields, i.e., for **M** fully aligned with the external field, and the pure AMR geometry with zero (antisymmetric) Hall signal, i.e., for **M** oriented in the plane of the device. (Ga,Mn)As films grown on the (001)-GaAs substrate will be considered.

The phenomenological decomposition of the AMR of (Ga,Mn)As into various terms allowed by symmetry is obtained by extending the standard phenomenology

[112], to systems with the cubic [100] plus the uniaxial [110] anisotropy. With this the longitudinal AMR is written as [108]

$$\frac{\Delta\rho_{xx}}{\rho_{av}} = C_I \cos 2\phi + C_U \cos 2\psi + C_C \cos 4\psi + C_{I,C} \cos(4\psi - 2\phi), \tag{2}$$

where $\Delta\rho_{xx} = \rho_{xx} - \rho_{av}$, ρ_{av} is the ρ_{xx} averaged over 360° in the plane of the film, ϕ is the angle between the magnetization unit vector $\hat{\mathbf{M}}$ and the current $\mathbf{I}$, and ψ is the angle between $\hat{\mathbf{M}}$ and the [110] crystal direction. The four contributions are the noncrystalline term, the lowest order uniaxial and cubic crystalline terms, and a crossed noncrystalline/crystalline term. The purely crystalline terms are excluded by symmetry for the transverse AMR, and one obtains

$$\frac{\Delta\rho_{xy}}{\rho_{av}} = C_I \sin 2\phi - C_{I,C} \sin(4\psi - 2\phi). \tag{3}$$

In the dilute-moment systems like (Ga,Mn)As ferromagnets, two distinct microscopic mechanisms lead to anisotropic carrier lifetimes. One combines the spin–orbit coupling in the carrier band with polarization of randomly distributed magnetic scatterers and the other with polarization of the carrier band itself resulting in an asymmetric band-spin texture. Although acting simultaneously in real systems, theoretically both mechanisms can be turned on and off independently. Since the former mechanism clearly dominates in (Ga,Mn)As, the spin splitting of the valence band is neglected in the following qualitative discussion. This is further simplified by focusing on the noncrystalline AMR in the heavy-hole Fermi surfaces in the spherical, $\mathbf{s} \parallel \mathbf{k}$, spin-texture approximation [113] and considering scattering off a δ-function potential $\propto \left(r + \hat{\mathbf{M}} \cdot \mathbf{s}\right)$. Here $\mathbf{s}$ and $\mathbf{k}$ are the carrier spin operator and wave vector, and r represents the ratio of nonmagnetic and magnetic parts of the Mn impurity potential. Assuming a proportionality between conductivity and lifetimes of carriers with $\mathbf{k} \| \mathbf{I}$ gives the following qualitative analytical expression for the AMR in this class of materials [108],

$$\frac{\sigma\left(\hat{\mathbf{M}} \parallel \mathbf{I}\right)}{\sigma\left(\hat{\mathbf{M}} \perp \mathbf{I}\right)} = \left(r^2 + \frac{1}{4}\right)\left(r^2 + \frac{1}{12}\right)\left(r^2 - \frac{1}{4}\right)^{-2}. \tag{4}$$

Therefore, when $r \ll 1$, one expects $\sigma\left(\hat{\mathbf{M}} \parallel \mathbf{I}\right) < \sigma\left(\hat{\mathbf{M}} \perp \mathbf{I}\right)$ (as is usually observed in metallic ferromagnets). However, the sign of the noncrystalline AMR reverses at a relatively weak nonmagnetic potential ($r = /\sqrt{20}$ in the model), its magnitude is then maximized when the two terms are comparable ($r = 1/2$), and, for this mechanism, it vanishes when the magnetic term is much weaker than the nonmagnetic term ($r \to \infty$).

Physically, carriers moving along $\hat{\mathbf{M}}$, i.e., with $\mathbf{s}$ parallel or antiparallel to $\hat{\mathbf{M}}$, experience the strongest scattering potential among all Fermi surface states when

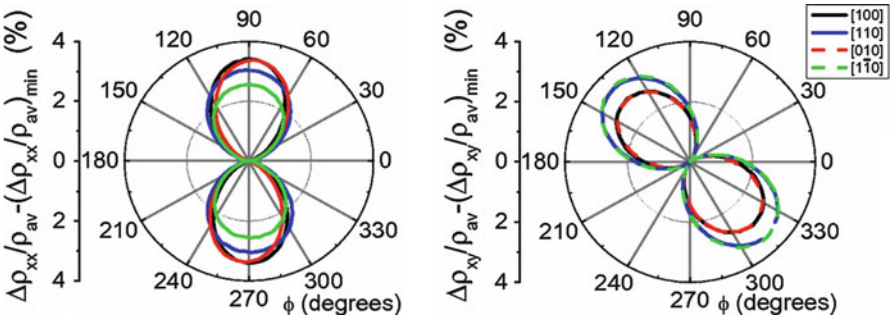

Fig. 10 Measured (at 4.2 K) longitudinal and transverse AMR for $Ga_{0.92}Mn_{0\cdot05}As$ as a function of the angle between $\hat{\mathbf{M}}$ and **I**. The legend shows the direction of the current. The y-axes show that $\Delta\rho/\rho_{av}$ shifted such that the minimum is at zero (From Ref. [108]. Reprinted with permission from W. Limmer et al., Physical Review B, 74, 2006. Copyright (2006) by the American Physical Society)

$r = 0$, giving $\sigma(\hat{\mathbf{M}} \parallel \mathrm{I}) < \sigma(\hat{\mathbf{M}} \perp \mathrm{I})$. When the nonmagnetic potential is present, however, it can more efficiently cancel the magnetic term for carriers moving along $\hat{\mathbf{M}}$ and for relatively small r, the sign of AMR flips. Since $r < 1/\sqrt{20}$ is unrealistic for the magnetic acceptor Mn in GaAs [51, 111], one obtains $\sigma(\hat{\mathbf{M}} \parallel \mathrm{I}) < \sigma(\hat{\mathbf{M}} \perp \mathrm{I})$, consistent with experiment.

Differences among experimental AMRs for current along the [100], [110], and $[1\bar{1}0]$ directions show that cubic and uniaxial crystalline terms are also sizable. This phenomenology is systematically observed in experimental AMRs of weakly or moderately compensated metallic (Ga,Mn)As films. Typical data for such systems [108], represented by the 25 nm $Ga_{0.95}Mn_{0.05}As$ film with 3.6% AMR, are shown in Fig. 10 for the Hall bars patterned along the [100], [010], [110], and $[1\bar{1}0]$ directions.

The high crystalline quality metallic (Ga,Mn)As samples allow to produce low contact resistant Hall bars accurately orientated along the principle crystallographic axes, from which it is possible to extract the independent contributions to the AMR. It is also possible to fabricate low contact resistance Corbino disk samples for which the averaging over the radial current lines eliminates all effects originating from a specific direction of the current [108]. Corbino measurements are possible in these materials because they are near-perfect single crystals but with low carrier density and mobility (compared with single-crystal metals) and so can have large source-drain resistances compared with the contact resistances.

Measured results for a Corbino device fabricated from the same 25 nm $Ga_{0.95}Mn_{0.05}As$ film as used for the Hall bars are shown in Fig. 11 [108]. The AMR signal is an order of magnitude weaker than in the Hall bars and is clearly composed of a uniaxial and a cubic contribution. Figure 11 also shows the crystalline components of the AMR extracted by fitting the Hall bar data to the phenomenological longitudinal and transverse AMR expressions. Figure 11d shows the consistency for the coefficients $C_{I,C}$, C_U, and C_C when extracted from the Hall bar

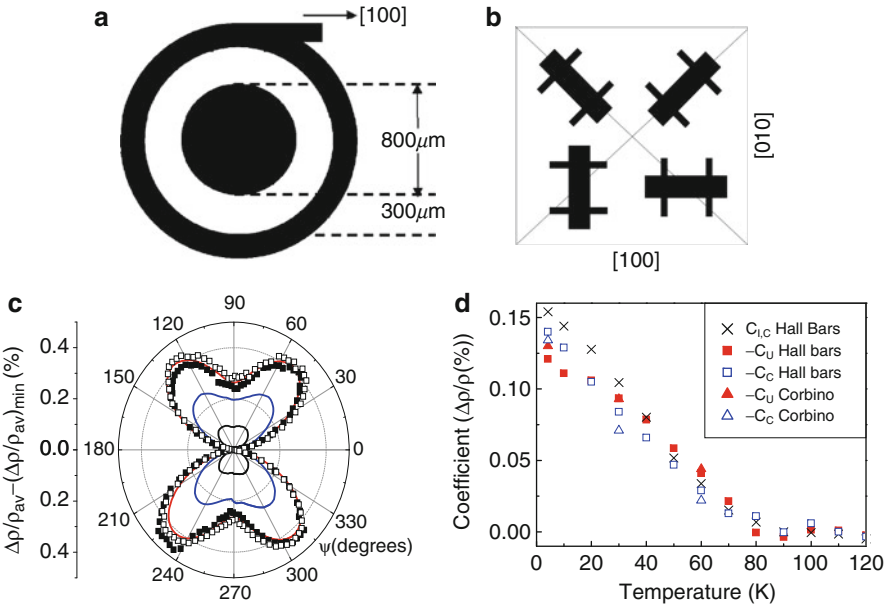

Fig. 11 (**a**) and (**b**) Cartoons of the Corbino disk and Hall bar devices, respectively. (**c**) MR of the 25 nm $Ga_{0.95}Mn_{0.05}As$ film in the Corbino geometry at 4.2 K (*red line*), 30 K (*blue line*), and 60 K (*black line*) and the crystalline component extracted from the Hall bars $\left(\mathrm{AMR}[110] + \mathrm{AMR}\left[1\bar{1}0\right]\right)/2$ (*closed points*) and (AMR[100] + AMR[010])/2 (*open points*). (d) Temperature dependence of the crystalline terms extracted from the Hall bars and Corbino devices (From Ref. [108]. Reprinted with permission from W. Limmer et al., Physical Review B, 74, 2006. Copyright (2006) by the American Physical Society)

and Corbino disk data over the whole range up to the Curie temperature (80 K). The uniaxial crystalline term, C_U, becomes the dominant term for $T \geq 30$ K. This correlates with the uniaxial component of the magnetic anisotropy which dominates for $T \geq 30$ K as observed by SQUID magnetometry measurements [108, 114].

A unique AMR phenomenology has been observed on ultrathin (5 nm) $Ga_{0.95}Mn_{0.05}As$ films [108]. The crystalline terms dominate the AMR with the uniaxial crystalline term being the largest. SQUID magnetometry on 5 nm $Ga_{0.95}Mn_{0.05}As$ films consistently shows that the uniaxial component of the magnetic anisotropy dominates over the whole temperature range [115]. The 5 nm films have lower Curie temperatures ($T_C \approx 30$ K) than the 25 nm films and become highly resistive at low temperature, indicating that they are close to the metal–insulator transition. The strength of the effect in the 5 nm films is remarkable, and it is not captured by theory simulations assuming weakly disordered, fully delocalized (Ga,Mn)As valence bands. It might be related to the expectation that magnetic interactions become more anisotropic with increasing localization of the holes near their parent Mn ions as the metal–insulator transition is approached [51].

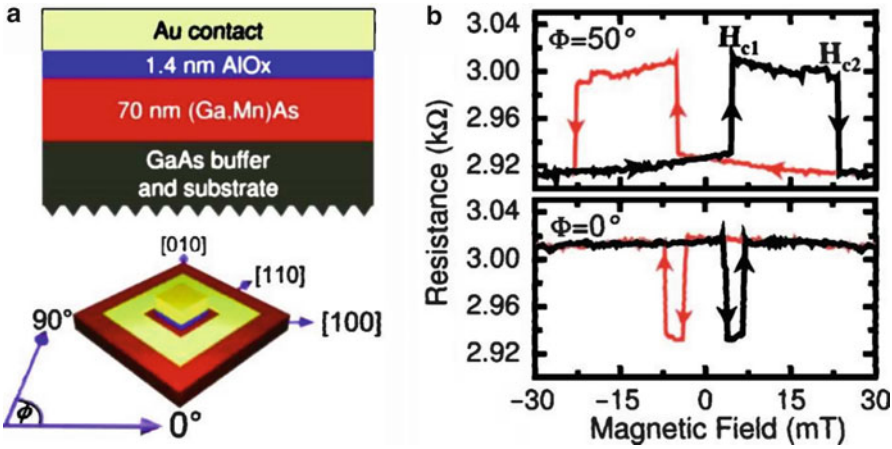

Fig. 12 (**a**) Schematic showing layer structure, contact geometry, and crystallographic directions in the TAMR device. (**b**) Magnetoresistance (MR) hysteresis curves for $T = 4.2$ K and 1 mV bias with in-plane magnetic field H along 0° and 50°. MR is spin valve like with two abrupt switching events at H_{c1} and H_{c2}. Depending on the angle, the width of the feature and, more important, its sign can change. The high-resistance state corresponds to magnetization along [100]-axis and the low-resistance state along [010]-axis (Reprinted with permission from [129]. Copyright (2005), AIP Publishing LLC)

Tunnel Junctions

The tunneling magnetoresistance (TMR) represents the difference between resistivities in configurations with parallel and antiparallel polarizations of ferromagnetic layers separated by a nonmagnetic barrier in magnetic tunnel junctions [99, 116–119]. The TMR in tunnel junctions can be much larger than the AMR of simple ohmic resistors and is the key effect utilized for readout in modern MRAMs [120].

In (Ga,Mn)As, functional magnetic tunnel junction devices can be built, as demonstrated by the measured large TMR effects [20–24, 121–125]. Here we focus on the physics of the tunneling anisotropic magnetoresistance (TAMR) which was discovered in (Ga,Mn)As-based tunnel devices [22, 39, 121, 122, 125–128]. TAMR, like AMR, arises from spin–orbit coupling and reflects the dependence of the tunneling density of states of the ferromagnetic layer on the orientation of the magnetization. The effect does not rely on spin coherence in the tunneling process and requires only one ferromagnetic contact.

In Fig. 12 we show the TAMR signal which was measured in a (Ga,Mn)As/AlO_x/Au vertical tunnel junction [39, 129]. For the in-plane magnetic field applied at an angle 50° off the [100]-axis, the magnetoresistance is reminiscent of the conventional spin-valve signal with hysteretic high-resistance states at low fields and low-resistance states at saturation. Unlike the TMR, however, the sign changes when the field is applied along the [100]-axis. Complementary SQUID

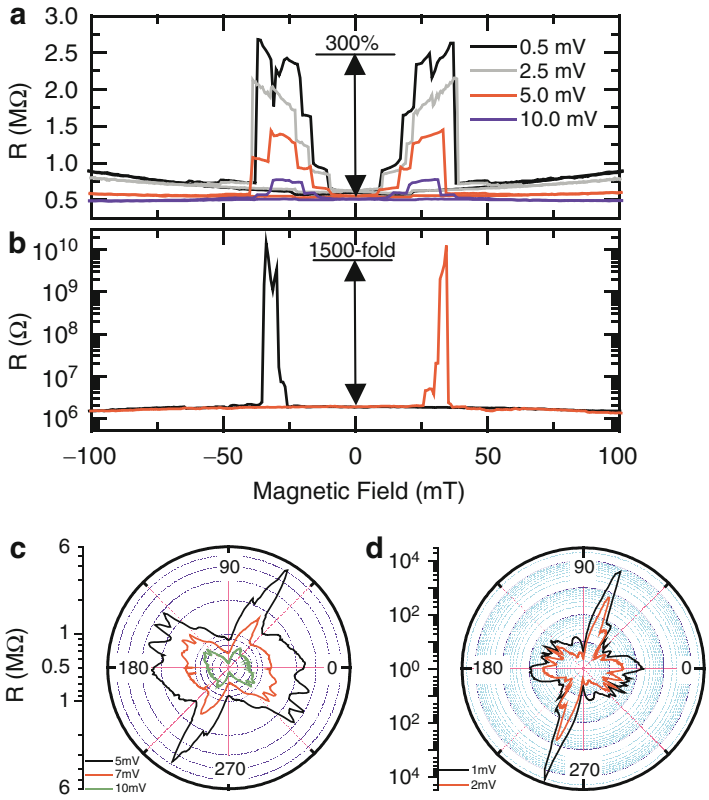

Fig. 13 (**a**) TAMR along $\phi = 65°$ at 4.2 K for various bias voltages. (**b**) Very large TAMR along $\phi = 95°$ at 1.7 K and 1 mV bias. (**c**) and (**d**) ϕ at various bias at 1.7 K (From Ref. [126]. Reprinted with permission from C. Rüster et al., Physical Review Letters, 94, 2005. Copyright (2005) by the American Physical Society)

magnetization measurements confirmed that for the sample measured in Fig. 12, the high-resistance state corresponds to magnetization in the (Ga,Mn)As contact aligned along the [100]-direction and the low-resistance state along the [010]-direction and that this TAMR effect reflects the underlying magnetocrystalline anisotropy between the $\mathbf{M} \parallel [100]$ and $\mathbf{M} \parallel [010]$ magnetic states of the specific (Ga,Mn)As material used in the study. Since the field is rotated in the plane perpendicular to the current, the Lorentz force effects on the tunnel transport can be ruled out. Microscopic calculations consistently showed that the spin–orbit coupling-induced density-of-state anisotropies with respect to the magnetization orientation can produce TAMR effects in (Ga,Mn)As of the order ~1 % to ~10 % [39, 129].

At very low temperatures and bias voltages, huge TAMR signals were observed [129] in a (Ga,Mn)As/GaAs/(Ga,Mn)As tunnel junction (see Fig. 13) which are not described by the one-body theories of anisotropic tunneling transmission

coefficients. The observation was interpreted as a consequence of electron–electron correlation effects near the metal–insulator transition [130]. Large anisotropic magnetoresistance effects were also measured in lateral nano-constriction devices fabricated in ultrathin (Ga,Mn)As materials [131–133]. The comparison of the anisotropic magnetoresistance signals in the unstructured part of the device and in the nano-constriction showed a significant enhancement of the signal in the constriction [131]. Subsequent studies of these nano-constrictions with an additional side gate patterned along the constriction, discussed in detail in section "Transistors" [10, 42, 134, 135], indicated that single-electron charging effects were responsible for the observed large anisotropic magnetoresistance signals.

Capacitors

Classifying magnetocapacitance along similar lines as magnetoresistance, both ordinary and spin-dependent effects have been observed in various systems. Changes in capacitance as a function of in-plane magnetic field were measured in two-dimensional electron gases and attributed to combined Lorentz force and quantum confinement effects [136, 137]; spin-dependent effects were measured due to the Zeeman splitting in Pd plate capacitors [138], and in magnetic tunnel junctions, several measurements have shown changes in capacitance as a function of relative magnetization orientation [139–141]. Research in (Ga,Mn)As has led to the discovery of the third class, the anisotropic magnetocapacitance whose origin is in the spin–orbit interaction [142].

Figure 14 shows the capacitor stack with one of the electrodes made of (Ga,Mn)As, the equivalent circuit, and the measured complex admittance of the capacitor.

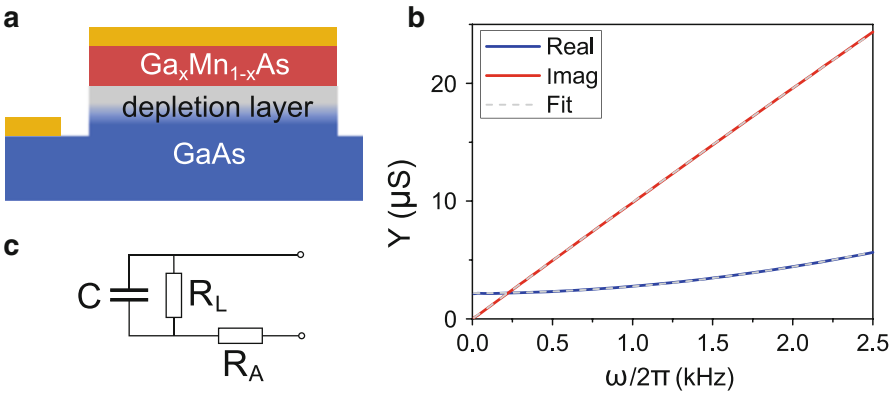

Fig. 14 (**a**) (Ga,Mn)As magnetocapacitance device structure. (**b**) Example measurement and fit of admittance of (Ga,Mn)As p–n junction capacitor. The leakage resistance and the access resistance are evident in the offset and frequency dependence of the real part, respectively. (**c**) Lumped element circuit diagram used for fitting (From Ref. [142]. Reprinted with permission from J. A. Haigh et al., Physical Review B, 91, 2015. Copyright (2015) by the American Physical Society)

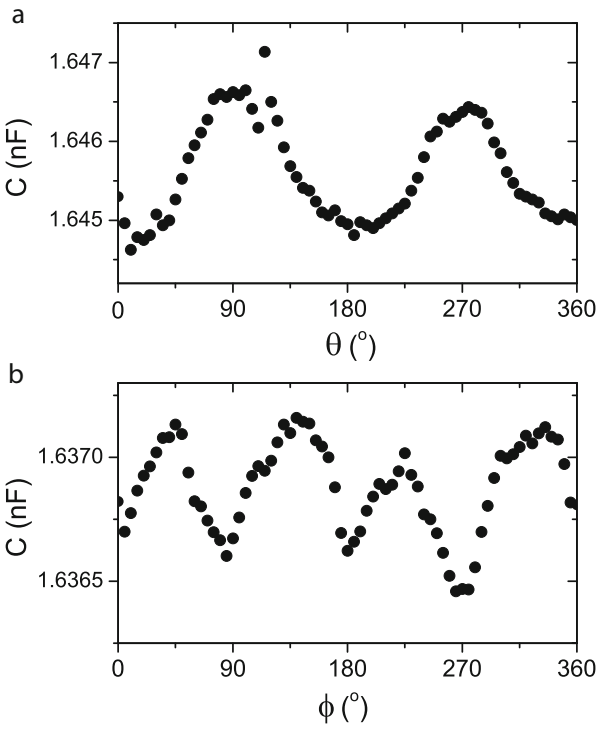

Fig. 15 2 K measurements of magnetocapacitance for rotations of the magnetization (**a**) out of plane and (**b**) in plane with a 1 T magnetic field. The capacitance is extracted from the fitting of the complex admittance (From Ref. [142]. Reprinted with permission from J. A. Haigh et al., Physical Review B, 91, 2015. Copyright (2015) by the American Physical Society)

In Fig. 15 the capacitance is plotted as a function of in-plane (a) and out-of-plane (b) magnetic-field orientation. There is a clear cubic in-plane symmetry and uniaxial out-of-plane symmetry to the change in capacitance. This is the symmetry that might be expected due to the bulk cubic crystal symmetry in the plane and uniaxial out-of-plane anisotropy due to the compressive strain on the (Ga,Mn)As epilayer grown on the GaAs substrate.

Based on the Thomas–Fermi screening length, one can formulate an effective "kinetic" capacitance, in series to the conventional geometric capacitance, with a dependence on the DOS [143]:

$$C_k/A = \sqrt{e^2 \epsilon_0 \epsilon_{eff} \rho_{3D}} \tag{5}$$

where ρ_{3D} is the DO, $\epsilon_0 \epsilon_{\text{eff}}$ is the effective dielectric constant of the constant material, and A is the area of the plate. Taking $\rho_{3D} \approx 10^{46}\ \text{J}^{-1}\text{m}^{-3}$ from independent DOS measurements in (Ga,Mn)As [144], $C_k/A \approx 50\text{fF}\mu\text{m}^{-2}$. The change in the total capacitance of the device C_T can be related to the change in the kinetic capacitance by

$$\frac{\Delta C_T}{C_T} = \frac{C_T}{C_k} \frac{\Delta C_k}{C_k}. \tag{6}$$

It can be seen from this equation that increasing the ratio of total to kinetic capacitance would increase the size of the modulation when rotating the magnetization vector in the ferromagnet. The total capacitance per area of the studied device is $\approx$ 2fF μm^{-2}. From these values a $\approx$ 5% change in the DOS would be needed to explain the 0.1 % anisotropic magnetocapacitance measured for the out-of-plane field rotation, a value which is reasonable in the studied (Ga,Mn)As material.

Transistors

Magnetically induced changes in the position of the chemical potential can be used to construct field-effect transistors whose channel conductance is controlled by spin-dependent effects in the electrodes. Shifts in the chemical potential associated with the magnetic-field-induced Zeeman splitting of the ferromagnetic bands were observed in single-electron transistor (SET) devices as spin-dependent magneto-Coulomb oscillations [145, 146]. Research in (Ga,Mn)As-based SETs has led to the discovery of the relativistic Coulomb-blockade (CB) AMR [10, 42, 44, 134, 135].

Ferromagnetic SETs with (Ga,Mn)As in the transport channel of the transistor [42, 135] were fabricated by trench-isolating a side-gated narrow channel in a thin-film (Ga,Mn)As epilayer (see Fig. 16). The nonuniform carrier concentration produces differences between chemical potentials $\Delta\mu$ of the lead and of the island in the constriction. There are two mechanisms through which $\Delta\mu$ depends on the magnetic field. One is caused by the direct Zeeman coupling of the external

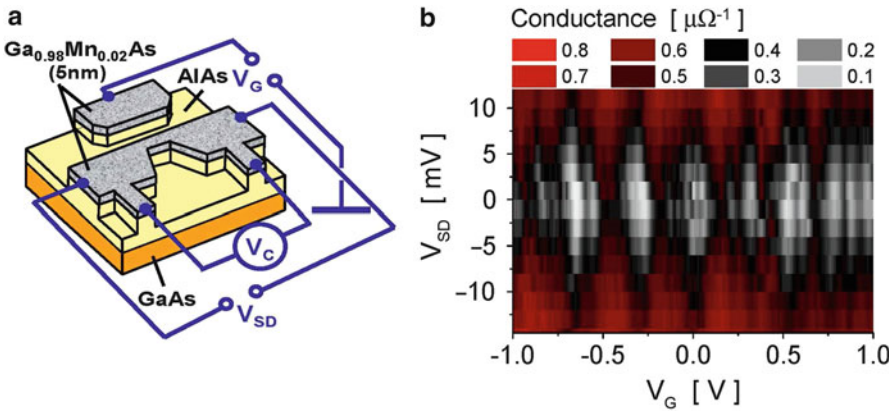

Fig. 16 (**a**) Schematics of an all-(Ga,Mn)As SET. Trench-isolated side gate and channel aligned along the [110] direction were patterned in a 5 nm $Ga_{0.98}Mn_{0.02}As$ epilayer. (**b**) CB conductance (I/V_C) oscillations with gate voltage for different source-drain bias. The diamond patterns in this 2D plot are clear fingerprints of single-electron transport (From Ref. [42]. Reprinted with permission from J. Wunderlich et al., Physical Review Letters, 97, 2006. Copyright (2006) by the American Physical Society)

magnetic field and leads to a CB magnetoresistance previously observed in ferromagnetic metal SETs [147].

The CB-AMR effect, discovered in the (Ga,Mn)As SETs, is attributed to the spin–orbit coupling-induced anisotropy of the carrier chemical potential, i.e., to magnetization orientation-dependent differences $\Delta\mu(\mathbf{M})$ between chemical potentials of the lead and of the island in the constriction [42]. A marked shift in the CB oscillation pattern is observed when $|\Delta\mu(\mathbf{M})|$ is of the order of the island single-electron charging energy. The fact that CB-AMR occurs when the anisotropy in a band structure-derived parameter is comparable to an independent scale (single-electron charging energy) makes the effect distinct and potentially much larger in magnitude as compared to the AMR and TAMR. Indeed, resistance variations by more than three orders of magnitude were observed in the (Ga,Mn)As SETs.

The sensitivity of the magnetoresistance to the orientation of the applied magnetic field is an indication of the anisotropic magnetoresistance origin of the effect. This is confirmed by the observation of comparably large and gate-controlled magnetoresistance in a field-sweep experiment and when the saturation magnetization is rotated with respect to the crystallographic axes. The field-sweep and rotation measurements are shown in Fig. 17c, d and compared with analogous measurements of the ohmic AMR in the unstructured part of the (Ga,Mn)As bar, plotted in Fig. 17a, b [42]. In the unstructured bar, higher or lower resistance states correspond to magnetization along or perpendicular to the current direction. Similar behavior is seen in the SET part of the device at, for example, $V_G = -0.4$ V, but the anisotropic magnetoresistance is now hugely increased and depends strongly on the gate voltage.

The huge magnetoresistance signals can be also hysteretic which shows that CB-AMR SETs can act as a nonvolatile memory/transistor element. In nonmagnetic SETs, the CB "on" (low resistance) and "off" (high resistance) states can represent logical "1" and "0," and the switching between the two states can be realized by applying a gate voltage, in analogy with a standard field-effect transistor. The CB-AMR SET can be addressed also magnetically with comparable "on" to "off" resistance ratios in the electric and magnetic modes.

Anther type of a (Ga,Mn)As SET device [44] is shown in Fig. 18. Here the SET has a micron-scale Al island separated by aluminum oxide tunnel junctions from Al source and drain leads (Fig. 18a). It is fabricated on top of a (Ga,Mn)As layer, which is electrically insulated from the SET by an alumina dielectric, and acts as a spin back gate to the Al SET. By sweeping the externally applied potential to the SET gate (Vg), one obtains the conductance oscillations that characterize the CB, as shown in Fig. 18b. Due to the magnetic gate, a shift is observed in these oscillations by an applied saturating magnetic field which rotates the magnetization in the (Ga, Mn)As gate. Figure 18b shows measurements for the in-plane ($\Phi = 90^\circ$) and for the perpendicular-to-plane ($\Phi = 0^\circ$) directions of magnetization. Alternatively, Fig. 18c shows the channel conductance as a function of the magnetization angle Φ for a fixed external potential V_g applied to the gate. The oscillations in Φ seen in Fig. 18c are of comparable amplitude as the oscillations in V_g in Fig. 18b.

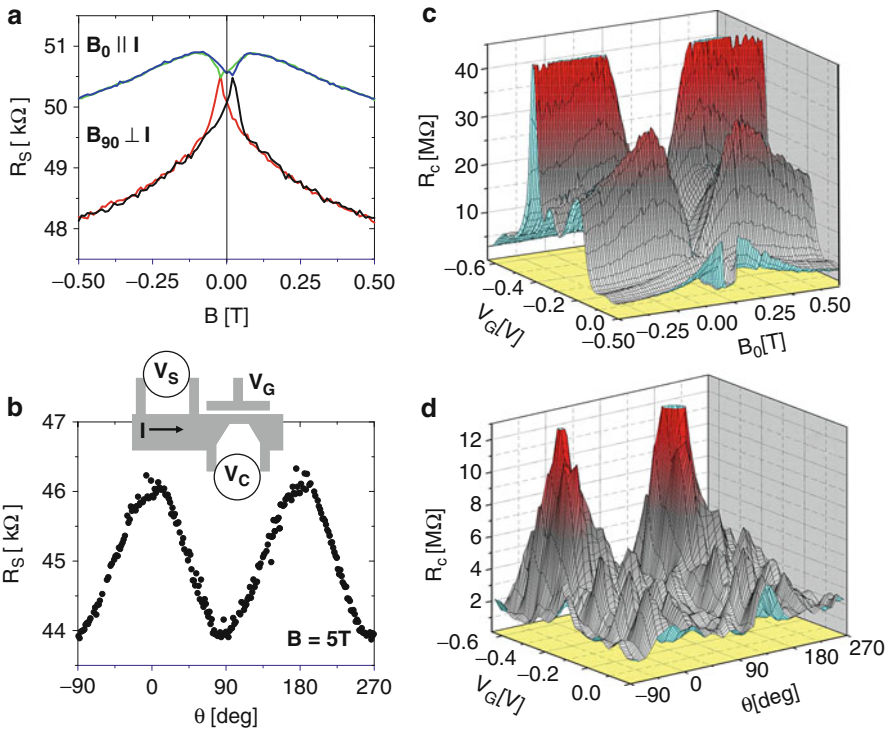

Fig. 17 (**a**) Resistance $R_S = V_S/I$ of the unstructured bar (see schematic diagram) versus up and down sweeps of in-plane magnetic field parallel (*blue*/*green*) and perpendicular (*red*/*black*) to the current direction. (**b**) R_S versus the angle between the current direction and an applied in-plane magnetic field of 5 T, at which **M** ∥ **B**. (**c**) Channel resistance R_C versus gate voltage and down sweep of the magnetic field parallel to the current. (**d**) R_C vs. gate voltage and the angle between the current direction and an applied in-plane magnetic field of 5 T (From Ref. [42]. Reprinted with permission from J. Wunderlich et al., Physical Review Letters, 97, 2006. Copyright (2006) by the American Physical Society)

Since the (Ga,Mn)As back gate is attached to a charge reservoir, any change in the internal chemical potential of the gate induced by the rotating magnetization vector causes an inward, or outward, flow of charge in the gate, as illustrated in Fig. 18e. This change in back-gate charge offsets the Coulomb oscillations (Fig. 18b) and changes the conductance of the nonmagnetic transistor channel for a fixed external potential applied to the gate (Fig. 18c).

The device clearly derives its functionality from the oldest among spintronics phenomena, namely, from the AMR. Simultaneously it appears to violate the established definition of spintronics as a portmanteau meaning "spin transport electronics." In the device shown in Fig. 18, the transport channel is nonmagnetic, and all the spin action is encoded in the capacitively coupled magnetic gate electrode.

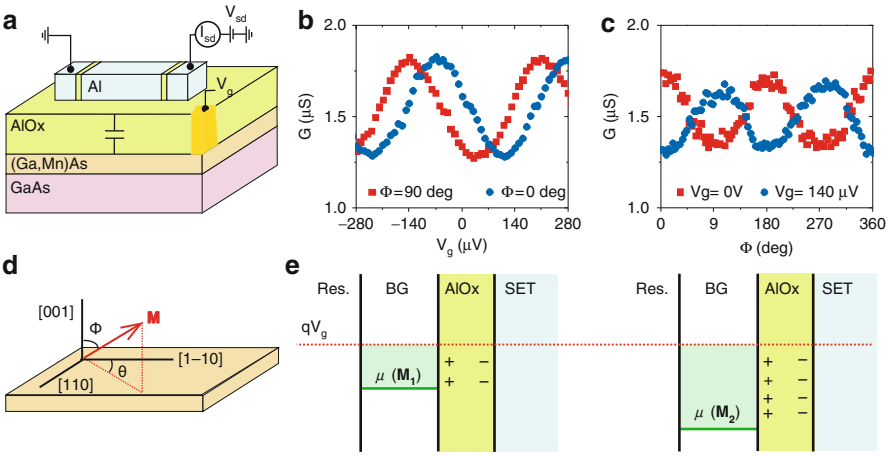

Fig. 18 (**a**) Schematic showing the SET channel separated by AlO_x dielectric from the ferromagnetic (Ga,Mn)As back gate. The SET comprises Al leads and island and AlO_x tunnel barriers. (**b**) Coulomb oscillations for the SET on $Ga_{0.97}Mn_{0.03}As$ for *two* different polar angles Φ of the magnetization. (**c**) Magneto-Coulomb oscillations shown by the same SET by varying the angle of magnetization for *two* different gate voltages. (**d**) Magnetization vector with respect to (Ga,Mn)As crystal axes. (**e**) Schematic explaining the spin-gating phenomenon: reorientation of the magnetization from $\mathbf{M}_1$ to $\mathbf{M}_2$ causes a change in the chemical *potential* of the (Ga,Mn)As back gate (BG). This causes charge to flow onto the back gate from the reservoir (Res.). The net effect is to alter the charge on the back gate and therefore the SET conductance. The externally applied electrochemical *potential* on the gate $\mu_{ec} = qV_g$ is held constant (Reprinted with permission from [44]. Copyright (2012), AIP Publishing LLC)

Spin-Hall Magnetoresistance

We have mentioned in section "Resistors" that the first generation of magnetic random access memories (MRAMs) was based on the AMR. These MRAMs relied on magnetic fields not only for writing but also for reading the information in a uniaxial ferromagnet [110]. The Oersted field was employed for partially tilting the moments during readout and by this for breaking the symmetry between the opposite magnetization orientation states. Without the tilt, i.e., for moments flipped strictly by 180°, the AMR vanishes by symmetry. In modern MRAMs based on the TMR, the auxiliary Oersted field is removed from the readout scheme [148]. Instead, the symmetry breaking is provided by interfacing the storing free ferromagnet with a reference fixed ferromagnet.

Research in (Ga,Mn)As has led to the discovery [149] of a reading scheme for the 180° magnetization reversal which does not require a symmetry-breaking magnetic field or a reference ferromagnet [149, 150]. It is due to the so-called linear spin-Hall magnetoresistance (LSMR) [149] with the maximum and minimum resistance values corresponding to the opposite magnetization directions in the ferromagnet. In the studied structure, the ferromagnet is represented by a

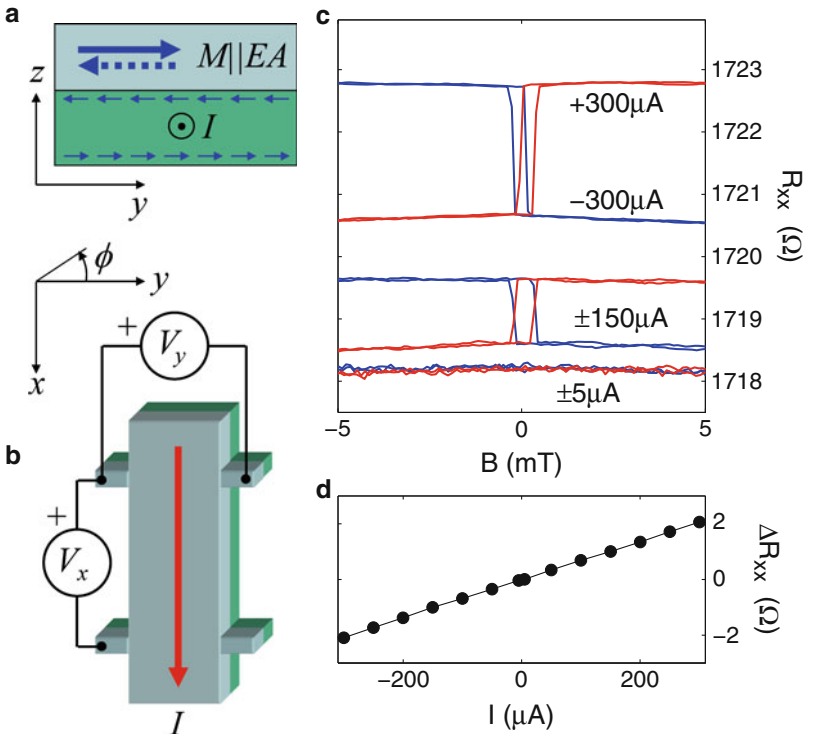

Fig. 19 (**a**) Schematic of the LSMR phenomenon. *Thin arrows* represent the SHE-induced spin polarization; *thick arrows* represent the easy-axis (EA) magnetization of the ferromagnet. (**b**) Schematic of the device and measurement geometry. (**c**) Longitudinal resistance measurements at 130 K and different amplitudes and signs of the applied current as a function of the external magnetic field. Steps correspond to the 180° magnetization reversal. (**d**) Difference between resistance states for opposite magnetizations, set by sweeping the magnetic field from negative or positive values to the zero field, as a function of the applied current (From Ref. [149]. Reprinted with permission from K. OlejnÚk et al., Physical Review B, 91, 2015. Copyright (2015) by the American Physical Society)

$Ga_{0.91}Mn_{0.09}As$ film with Curie temperature $T_{c1} = 155$ K. It is grown on top of a $Ga_{0.97}Mn_{0.03}As$ which remains paramagnetic down to $T_{c2} = 95$ K, has a similar conductivity as the top, higher Mn-doped film, and for which one expects a sizable spin-Hall effect (SHE) [151, 152]. This bilayer geometry implies that for the given in-plane current polarity, the SHE generates a fixed in-plane, perpendicular-to-current spin polarization at the interface with the ferromagnetic (Ga,Mn)As. When the axis of the in-plane magnetization of the ferromagnet is also transverse to the current, as illustrated in Fig. 19a, then flipping the sign of the magnetization results in the LSMR. The phenomenology can be viewed as analogous to the ferromagnetic bilayer structure operated in the in-plane current GMR geometry and with the fixed reference ferromagnet replaced in the structure with the paramagnetic SHE polarizer.

The measurement setup is shown in Fig. 19b and the magnetoresistances detected at 130 K are plotted in Fig. 19c, d. At a probe current of amplitude 5 μA, corresponding to current density of 1.25×10^4 Acm^{-2}, a negligible change in the longitudinal resistance R_{xx} is observed for the magnetic field swept along the easy axis, as shown in Fig. 19c. On the other hand, at 150 and 300 μA, a magnetoresistance signal is observed which increases with increasing current and is an odd function when reversing magnetization by 180°. The hysteretic R_{xx} jumps whose sign flips when flipping the field-sweep direction or the polarity of the probe current occur at ±0.2 mT which is the easy-axis coercive field. Figure 19d shows the difference between resistance states for opposite magnetizations set by sweeping the magnetic field from negative or positive values to the zero field. The difference increases linearly with the applied probe current and change sign for the opposite current polarity.

We note that the LSMR effect [149, 150] is related to another spin-Hall magnetoresistance which is quadratic in the spin-Hall angle [153]. In the latter effect, a spin current generated by the SHE is either absorbed at the interface with a ferromagnet when the SHE polarization is transverse to the magnetization or, in the parallel configuration, it is reflected. The reflected spin current generates an additional voltage via the inverse SHE which renormalizes the resistance of the device. Unlike the LSMR and like the AMR, this quadratic-in-SHE phenomenon is independent of the sign of the magnetization.

Current-Induced Torques

When spin-polarized carriers are injected into a magnetic region whose moments are misaligned with the injected spin polarization of the carriers, spin–transfer torques (STTs) can act on the magnetization of the ferromagnet [154]. The phenomena belong to an important area of spintronics research focusing on the means for manipulating magnetic moments by electric fields and are the basis of the emerging technologies for scalable MRAMs [120].

Theoretical description of STTs is simplified when the nonequilibrium spin density of carriers s and magnetization **M** of the ferromagnet are treated as separate degrees of freedom and when the timescales for the coupled dynamics of **s** and **M** are very different. Dilute-moment ferromagnetic semiconductors, and (Ga,Mn)As in particular, are model systems in which the first assumption is well justified microscopically. Saturation magnetization of the ferromagnet **M** is primarily due to Mn *d*-orbital local moments, while the carrier states near the top of the valence band (or bottom of the conduction band) are dominated by As *p*-orbitals (or Ga *s*-orbitals) [49, 51].

The timescale for the precession of the nonequilibrium carrier spin polarization in the exchange field of local moments, described by

$$\frac{d\mathbf{s}}{dt} = \frac{J_{\mathrm{ex}} cS}{\hbar}\mathbf{s} + \hat{\mathbf{M}}, \tag{7}$$

is $\tau_{ex} = \hbar/J_{ex}cS$, where J_{ex} is the carrier-local moment exchange coupling and $cS \equiv |\mathbf{M}|$. The timescale for the precession of local moments in the exchange field of the nonequilibrium carrier spin polarization, described by

$$\frac{cS\frac{d\hat{\mathbf{M}}}{dt} = cSJ_{ex}|\mathbf{s}|}{\hbar\hat{\mathbf{M}} \times \hat{\mathbf{s}},} \tag{8}$$

is $\hbar/J_{ex}|\mathbf{s}|$. Since $cS \gg |\mathbf{s}|$ is common in the STT experiments, the local moment dynamics is typically much slower than the nonequilibrium carrier spin dynamics [47, 154–157]. This allows one to phenomenologically describe STTs in two steps. In the first step, the fast dynamics of $\mathbf{s}$ is considered, and one looks for a steady-state component of the nonequilibrium carrier spin density, $\delta\mathbf{s}$. In the second step, $\delta\mathbf{s}$ is introduced into Eq. 8 in order to infer STTs acting on the magnetization $\mathbf{M}$ of the ferromagnet.

Phenomenologically, the nonequilibrium carrier spin dynamics in the presence of the exchange field of local moments and steady injection rate P of carriers with spin polarization vector $\hat{\mathbf{n}}$ misaligned with $\mathbf{M}$ is given by

$$\frac{d\mathbf{s}}{dt} = \frac{J_{ex}cS}{\hbar}\mathbf{s} \times \hat{\mathbf{M}} + P\hat{\mathbf{n}} - \frac{\mathbf{s}}{\tau_s}, \tag{9}$$

where the last term reflects a finite spin lifetime of the nonequilibrium carriers in the ferromagnet. Two components of STT can be distinguished when considering two limiting cases of Eq. 9 [47, 154–157]. One limit is when carrier spin lifetime τ_s is much larger than the precession time τ_{ex}. In this case, and assuming for simplicity $\hat{\mathbf{n}} \perp \hat{\mathbf{M}}$, the steady-state component of the nonequilibrium carrier spin polarization in the ferromagnet is oriented perpendicular to both $\hat{\mathbf{n}}$ and $\hat{\mathbf{M}}$ and $|\delta_{\mathbf{S}}|/\tau_{ex} = P$. This follows from the steady-state solution of Eq. 9 ($d\mathbf{s}/dt = 0$) in which the last term on the right-hand side is neglected, and the rate of tilt of the nonequilibrium carrier spin polarization due to precession in the exchange field of local moments (first term in Eq. 9) is canceled by the rate of the incoming carrier spin polarization (second term in Eq. 9). The steady-state carrier polarization $\delta\mathbf{s}$ produces STT acting on the magnetization,

$$cS\frac{d\hat{\mathbf{M}}}{dt} = P\hat{\mathbf{M}} \times \left(\hat{\mathbf{n}} \times \hat{\mathbf{M}}\right). \tag{10}$$

In this adiabatic STT the entire spin-angular momentum of the injected carriers is transferred to the magnetization, independent of τ_s, τ_{ex}, and other parameters of the system. The adiabatic STT has been considered since the seminal theory works [158, 159] on carrier-induced magnetization dynamics which opened a large field ranging from metal magnetic tunnel junctions switched by current to tunable oscillators [154] and ultrafast photomagnetic laser excitations of ferromagnetic semiconductors [47, 157].

In the opposite limit of $\tau_{\mathbf{s}} \ll \tau_{\mathrm{ex}}$, $\delta\mathbf{s}$ remains parallel to the injected spin polarization $\hat{\mathbf{n}}$, and its magnitude is a product of the spin injection rate and spin lifetime, $|\delta_{\mathbf{s}}| = P\tau_{\mathrm{s}}$. This follows from Eq. 9 in which the first term on the right-hand side is neglected. The resulting nonadiabatic STT [155],

$$cS\frac{d\hat{\mathbf{M}}}{dt} = \frac{\tau_{\mathrm{s}}}{\tau_{\mathrm{ex}}}P\left(\hat{\mathbf{M}} \times \hat{\mathbf{n}}\right), \tag{11}$$

is perpendicular to the adiabatic STT and has a magnitude $|\mathbf{s}|/\tau_{\mathrm{ex}} = P\tau_s/\tau_{\mathrm{ex}}$. For intermediate ratios $\tau_{\mathrm{ex}}/\tau_{\mathrm{s}}$, both the nonadiabatic and adiabatic torques can be present, and the ratio of their magnitudes (nonadiabatic to adiabatic) is given by $\beta = \tau_{\mathrm{ex}}/\tau_{\mathrm{s}}$ [155–157]. The nonadiabatic STT plays a crucial role in current-induced domain-wall (DW) motion [155, 156]. It allows for a nonzero mobility of DW in the low-current steady-flow regime, with the DW mobility proportional to β/α where α is the damping parameter [155, 156, 160, 161].

One of the sources of small τ_{s}, i.e., large nonadiabatic STT, is spin–orbit coupling. Remarkably, a related spin–orbit torque (SOT) produced by spin–orbit coupling and electrical current can occur even in uniformly magnetized systems [45, 46, 162–166]. The presence of SOT in uniform ferromagnets can be illustrated by considering linear-response transport theory in which the occupied states on the Fermi surface are redistributed by the applied electrical current. The redistribution combined with microscopic non-collinearity of spin expectation values on the spin–orbit coupled Fermi surface produces a nonequilibrium steady-state component of the carrier spin polarization in systems with broken inversion symmetry. When misaligned with the equilibrium magnetization, SOT acts on the magnetic moments [163, 164, 167]. SOT has been employed in current-assisted magnetization reversal experiments in uniformly magnetized ferromagnetic semiconductor and metal thin films [45, 165] and in all-electrical ferromagnetic resonance measurements of uniformly magnetized ferromagnetic semiconductor nanodevices [46], and recent studies of thin-film metal ferromagnets have proposed that SOT can enhance the mobility of current-driven DWs [168].

Ferromagnetic (III,Mn)V semiconductors represent an ideal experimental realization of the above model picture of the STT [169], as well as of SOT [45, 46, 163–166] phenomena. The strong exchange interaction is accompanied in these materials by a strong spin–orbit coupling, resulting in $\tau_s \sim \tau_{ex}$ and, therefore, in the expectation of significant contributions of both adiabatic and nonadiabatic STTs [28, 30, 33, 34] and of SOT. Another favorable feature of dilute-moment (III,Mn)V ferromagnets is their low saturation moment, as compared to conventional dense-moment metal ferromagnets. Together with the high degree of spin polarization of carriers, it implies that electrical currents required to excite magnetization by STT in ferromagnetic semiconductors are also comparatively low [24–27, 32]. The combination of low saturation moment and strong spin–orbit coupling has yet another key advantage which is the dominant role of magnetocrystalline anisotropy fields over the demagnetizing anisotropy fields [27]. It allows to control the stability of the internal DW structure in situ by a

piezoelectric stressor attached to the ferromagnetic semiconductor sample [31]. Similarly, the inversion symmetry-breaking terms in the spin–orbit coupled band structure of (Ga,Mn)As, responsible for SOT, can be controlled by the lattice-matching growth strain or strains introduced post-growth by microfabrication or piezoelectric stressors [46, 94].

Tunnel Junctions and Domain Walls

In magnetic tunnel junctions with (Ga,Mn)As electrode, STT-induced switching was observed [24] at current densities of the order $10^4 - 10^5$ Acm^{-2}, as shown in Fig. 20. This is consistent with theory expectations [32] predicting one to two orders of magnitude lower current densities than in the STT experiments in common dense-moment metal ferromagnets.

Critical currents of the order 10^5 Acm^{-2} for the DW motion in the creep regime have been reported and the effect thoroughly explored in perpendicularly magnetized (Ga,Mn)As thin-film devices [25, 26, 170]. The perpendicular magnetization geometry was achieved by growing the films under a tensile strain on a (In,Ga)As substrate and is particularly useful for the direct magneto-optical Kerr-effect imaging of the domains, as illustrated in Fig. 21.

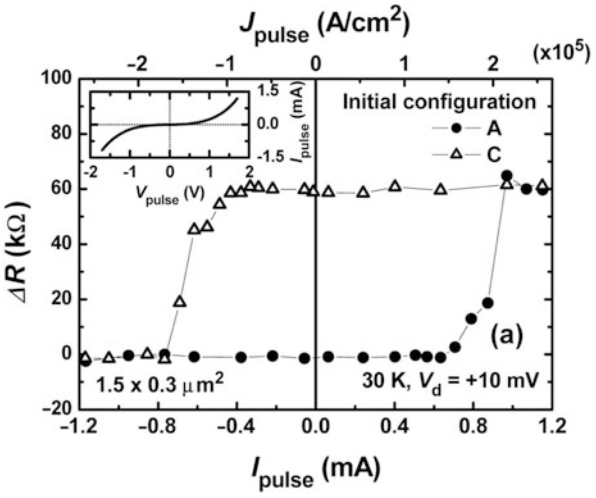

Fig. 20 (**a**) ΔR as a function of the applied current I_{pulse} of the 1.5 × 0.3 μm^2(Ga,Mn)As/GaAs/(Ga,Mn)As tunnel junction device at 30 K, where ΔR is the resistance difference between the resistance of the tunnel junction after application of I_{pulse} and parallel magnetization configuration. *Closed circles* show the I_{pulse} dependence of ΔR for initial configuration A (parallel magnetization), whereas *open triangles* show the results for initial configuration C (antiparallel magnetization). The *inset* shows $I-V$ characteristics of the device (From Ref. [24]. Reprinted with permission from D. Chiba et al., Physical Review Letters, 93, 2004. Copyright (2004) by the American Physical Society)

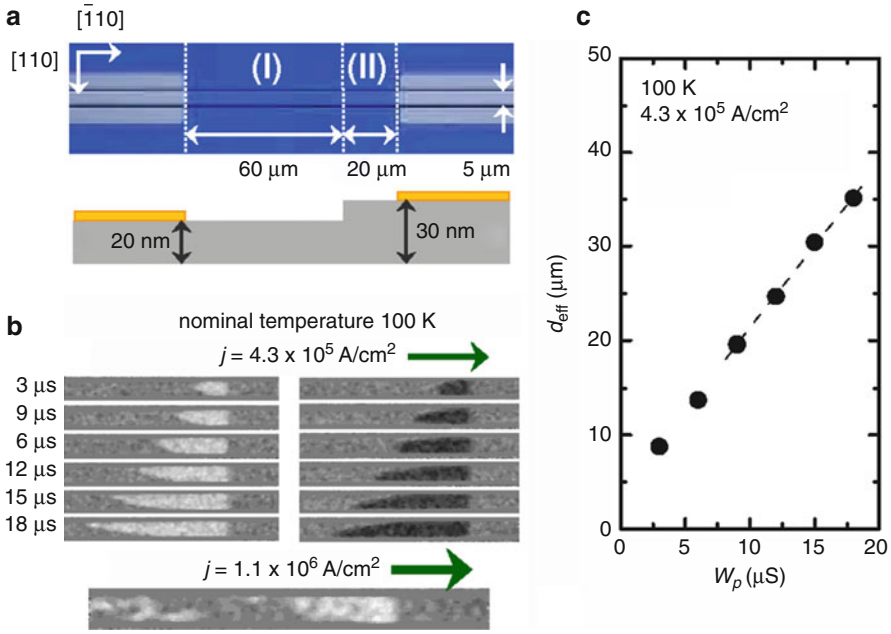

Fig. 21 (**a**) Layout of the device showing the 5 µm mesa and step for DW pinning in perpendicular magnetic anisotropy (Ga,Mn)As film. (**b**) 7 µm wide magneto-optical images with a 5 µm mesa in the center show *that* DW moves in the opposite direction to the current independent of the initial magnetization orientation and *that* DW displacement is proportional to pulse duration (**c**). The *lowest panel* in (**b**) shows destruction of ferromagnetic phase by Joule heating (From Ref. [26]. Reprinted with permission from M. Yamanouchi et al., Physical Review Letters, 96, 2006. Copyright (2006) by the American Physical Society)

The viscous-flow regime over a wide current range was achieved in high crystal quality (Ga,Mn)(As,P)/GaAs epilayers grown under tensile strain, resulting again in the out-of-plane easy axis [29–31]. The idea behind experiments shown in Fig. 22 is based on predictions of a simplified 1D model in which a Bloch (or Néel) DW in an out-of-plane magnetized system is assumed and in which the viscous-flow DW motion in a low-current steady regime is separated from a high-current precessional regime by the Walker breakdown (WB) [160, 161, 171]. The mobility (velocity divided by current) is larger below WB when the nonadiabatic STT is strong enough that $\beta/\alpha > 1$. For $\beta/\alpha < 1$, on the other hand, the DW mobility is larger above the WB threshold current.

The important property of the ferromagnetic semiconductor sample is that the position of the WB is governed by the uniaxial magnetocrystalline anisotropy field parallel to the magnetic epilayer plane and the rotation plane of the DW, whose magnitude can be tuned in a controlled way by applying bias voltage to an attached piezostressor [31, 36, 94, 172]. As a result, one can tune in situ the WB threshold

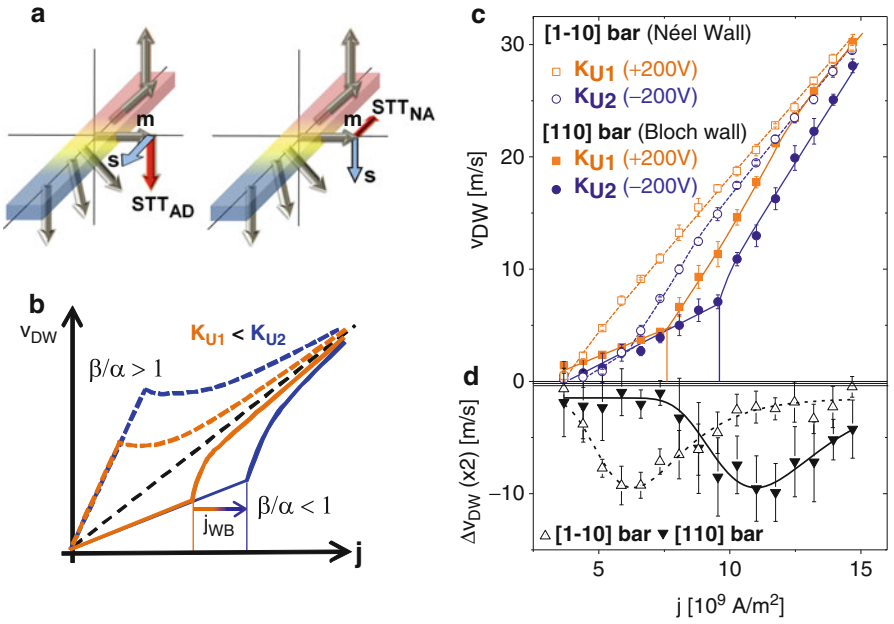

Fig. 22 (**a**) Illustration of the steady-state carrier spin polarization **s** and corresponding adiabatic STT (STT_{AD}) acting on magnetization **m** in the $\tau_s \gg \tau_{ex}$ limit (*left*) and nonadiabatic STT (STT_{NA}) in the $\tau_s \ll \tau_{ex}$ limit (*right*). (**b**) Schematic diagram of the predicted DW velocity as a function of the driving current in the presence of adiabatic and nonadiabatic STTs and $\beta/\alpha < 1$ or $\beta/\alpha > 1$ and of the predicted shift of the WB threshold current j_{WB} for *two* values of the in-plane magnetocrystalline constant $K_{u,1} < K_{u,2}$. (**c**) Measured DW velocity versus driving current density at piezo voltages −200 V or +200 V, strengthening or weakening the $[1\bar{1}0]$ in-plane easy axis, *respectively*. Open symbols correspond to the $[1\bar{1}0]$-oriented microbar with less internally stable Néel DW and filled symbols to the [110]-oriented microbar with *more* internally stable Bloch DW. The character of the measured data, including the shift of the WB threshold current, implies STTs with $\beta/\alpha < 1$. (*d*) $\Delta v_{DW} = v_{DW}\,(+200\text{ V}) - v_{DW}\,(-200\text{ V})$ *vs.* current density illustrates the piezoelectric control of the DW mobility achieved starting from lower currents in the $[1\bar{1}0]$-oriented microbar with less internally stable DW (From Ref. [31]. Copyright © 2013, Rights Managed by Nature Publishing Group)

current j_{WB} and the DW mobility and infer the β/α ratio which characterizes the strengths of adiabatic and nonadiabatic STTs in the studied magnet. The experimental realization of this proposal [172] is shown in Fig. 22c, d [31]. By comparing Fig. 22b, c, it can be concluded that both adiabatic and nonadiabatic STTs act in the current-driven DW motion experiments and that the characteristic ratio $\beta/\alpha < 1$. Figure 22d shows that by shifting the WB position one can control DW mobilities. Up to 500 % mobility variation, for an electrical-current-driven domain wall, have been observed in these piezoelectrically controlled DW STT experiments in (Ga, Mn)(As,P).

Uniform Magnets

The experimental discovery of SOT was reported in a (Ga,Mn)As sample whose image is shown in Fig. 23c [45]. The device was patterned into a circular island with eight nonmagnetic ohmic contacts (Fig. 23a). In the presence of a strong external magnetic field H, the magnetization of the ferromagnetic island is aligned with the field. For weak fields, however, the direction of magnetization is primarily determined by magnetic anisotropy. As a small field ($5 < H < 20$ mT) is rotated in the plane of the sample, the magnetization is realigned along the easy axis closest to the field direction. Such rotation of magnetization by an external field is demonstrated in Fig. 24. For the current $\mathbf{I} \parallel [1\bar{1}0]$, the measured transverse AMR (R_{xy}) is positive for $\mathbf{M} \parallel [100]$ and negative for $\mathbf{M} \parallel [010]$. The switching angles where R_{xy} changes

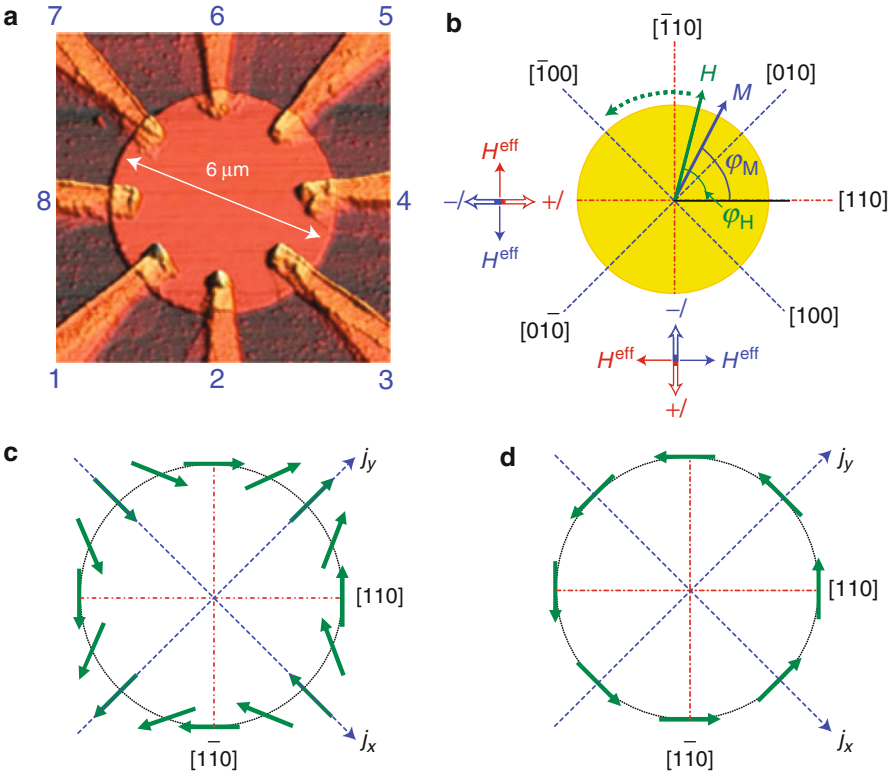

Fig. 23 (**a**) Atomic force micrograph of the studied sample with eight nonmagnetic metal contacts. (**b**) Diagram of device orientation with respect to crystallographic axes, with easy and hard magnetization axes marked with *blue dashed and red dot-dashed lines*, respectively. Measured directions of $\mathbf{H}_{eff}$ field are shown for different current directions. (**c**) and (**d**) Orientation of effective SOT field with respect to current direction for strain-induced (**c**) and Rashba (**d**) spin–orbit interactions (Reprinted by permission from Macmillan Publishers Ltd: Nature Physics [45], copyright (2009))

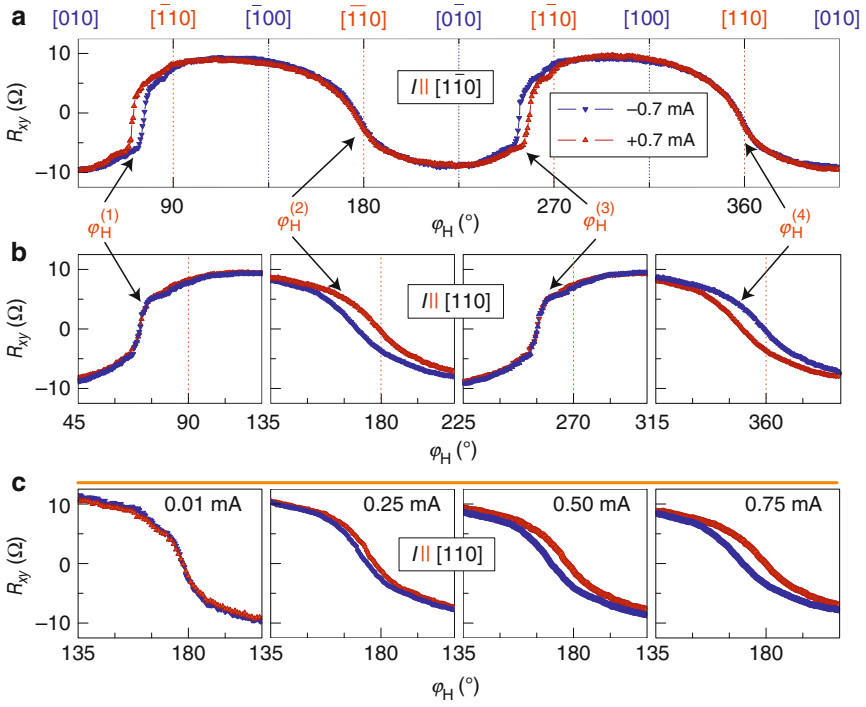

Fig. 24 (**a**) and (**b**) Transverse anisotropic magnetoresistance R_{xy} as a function of external field direction φ_H for $H = 10$ mT and current $I = \pm 0.7$ mA. The angles $\varphi_H^{(i)}$ mark magnetization switchings. (**c**) Magnetization switching between $[\bar{1}00]$ and $[0\bar{1}0]$ easy axes for several values of the current (Reprinted by permission from Macmillan Publishers Ltd: Nature Physics [45], copyright (2009))

sign are denoted as $\varphi_H^{(i)}$ on the plot. The data can be qualitatively understood if one considers an extra current-induced effective magnetic field H_{eff}, as shown schematically in Fig. 23b. The symmetry of the measured H_{eff} with respect to **I** coincides with the unique symmetry of the strain-related SOT field (Fig. 23c).

A form of ferromagnetic resonance (FMR) has been demonstrated based on SOT in which an electric current oscillating at microwave frequencies is used to create an effective SOT field in the magnetic material being probed, which makes it possible to characterize individual nanoscale samples with uniform magnetization profile [46]. Lithographically patterned (Ga,Mn)As and (Ga,Mn)(As,P) nanoscale bars were characterized, including broadband measurements of resonant damping as a function of frequency and measurements of anisotropy fields as a function of bar width and strain. In addition, vector magnetometry of these driving SOT fields revealed contributions with the symmetry of both the strain-related Dresselhaus SOT and of an additional Rashba-symmetry SOT.

The principle of the SOT-FMR technique is illustrated in Fig. 25a [46]. To drive the FMR, a microwave-frequency current was passed through the nanobar (Fig. 25b).

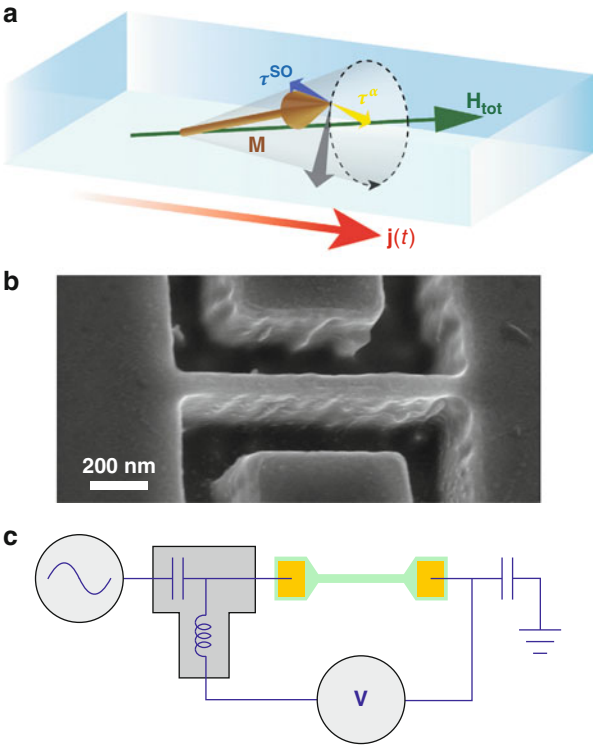

Fig. 25 (**a**) Precession of the magnetization vector **M** around the total magnetic field $\mathbf{H}_{tot}$. **M** is subject to a damping torque τ^{α} (*yellow arrow*) owing to energy dissipation, which causes the magnetic motion to relax toward $\mathbf{H}_{tot}$. The driving SOT τ^{SO} is due to the current-induced effective field. The current density vector is represented by $\mathbf{j}(t)$. (**b**) SEM image of an 80 nm wide bar, patterned from the (Ga,Mn)(As,P) wafer. (**c**) Schematic of the experimental setup. A microwave-frequency current is driven across the nanoscale magnetic bar, which is contacted with Cr/Au bondpads. The d.c. voltage, generated by magnetization precession, is extracted through a bias tee (represented by the capacitor and inductor network attached between the signal generator and sample source) (From Ref. [46]. Copyright © 2011, Rights Managed by Nature Publishing Group)

For detection, a frequency mixing effect based on AMR was used. When magnetization precession is driven, there is a time-dependent change $\Delta R(t)$ in longitudinal resistance from the equilibrium value R (owing to AMR). The resistance oscillates with the same frequency as the microwave current, thus causing frequency mixing, and a directly measurable d.c. voltage V_{dc} is generated. This voltage provides a direct probe of the amplitude and phase of magnetization procession with respect to microwave current.

Figure 26 presents measurements on an 80 nm wide nanobar patterned in the $[1\bar{1}0]$ direction from the (Ga,Mn)(As,P) epilayer. The magnetic-field dependence of V_{dc} is measured at different microwave frequencies. The frequency of the

incident current is fixed while an external d.c. magnetic field $\mathbf{H}_0$ is swept, and a well-defined resonance peak appears (Fig. 26a). The peak is well fitted by the solution of the Landau–Lifshitz–Gilbert (LLG) equation, which describes the dynamics of precessional motion of the magnetization.

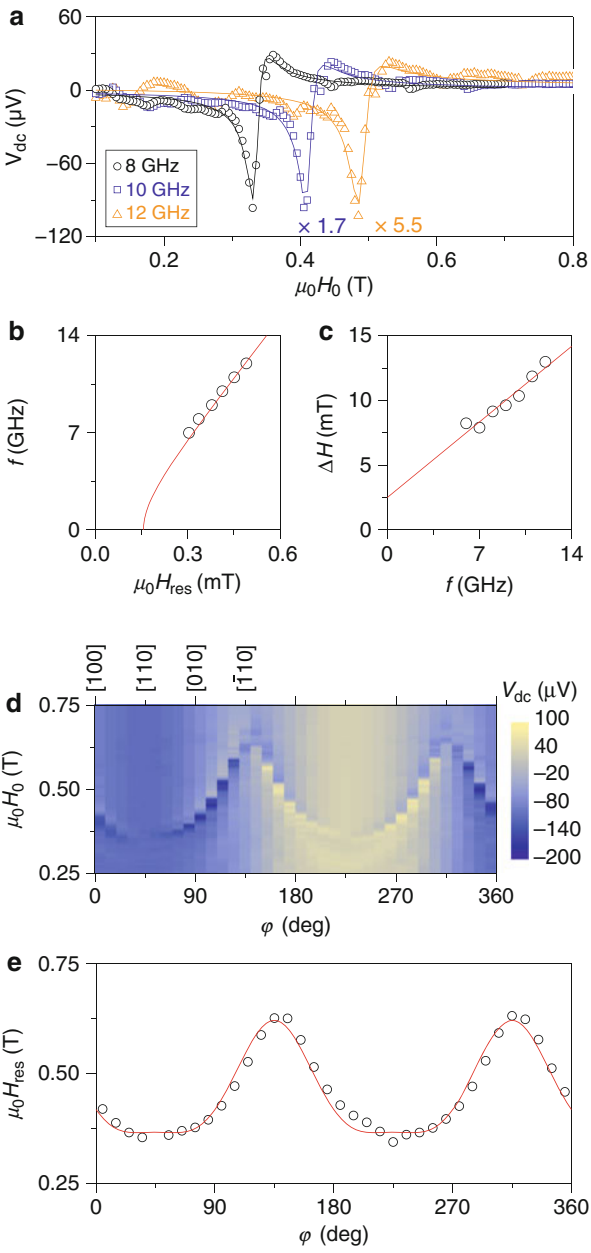

Fig. 26 (**a**) V_{dc} measured at 8, 10, and 12 GHz (*symbols*) on the 80 nm wide device. The resonance peaks are clearly observed and can be well described by the solution to the LLG equation. *Solid lines* are the fitted results. The difference in the signal level at different frequencies is caused by the frequency-dependent attenuation of the microwave circuit. (**b**) Resonance field H_{res} as a function of microwave frequency. The *red solid line* is the fitted result. (**c**) Frequency dependence of the FMR line width ΔH. The data are fitted to a *straight line* to extract ΔH_{inhomo} and α. (**d**) V_{dc} measured from in-plane rotational scans of the external field $\mathbf{H}_0$. The color scale represents the magnitude of the voltage. φ is the angle between the magnetization vector $\mathbf{M}$ and the [100] crystalline axis. (**e**) Angle plot of the resonance field H_{res}. The *red line* is a fitting curve to calculate the magnetic anisotropy (From Ref. [46]. Copyright © 2011, Rights Managed by Nature Publishing Group)

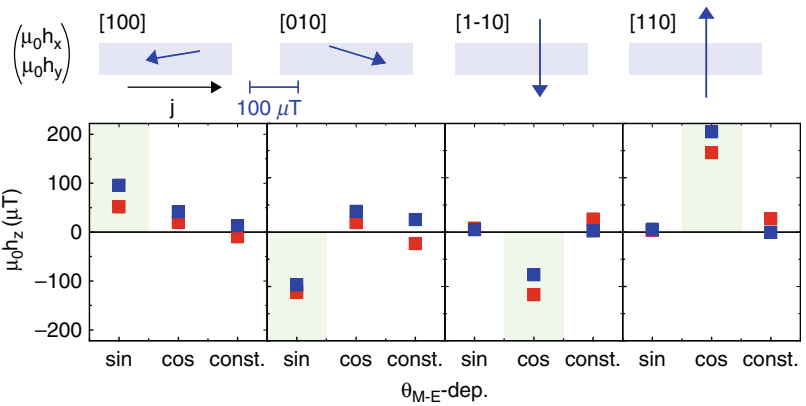

Fig. 27 Measured in-plane current-induced fields due to the field-like SOT and out-of-plane fields due to the anti-damping-like SOT in (Ga,Mn)As. In-plane spin–orbit field and coefficients of the cot θ_{M-E} and sin θ_{M-E} fit to the angle dependence on out-of-plane SOT field for our sample set. For the in-plane fields, a single sample in each microbar direction is shown (corresponding to the same samples that yield the blue out-of-plane data points). In the out-of-plane data, two samples are shown in each microbar direction. The symmetries expected for the anti-damping SOT, on the basis of the theoretical model for the Dresselhaus term in the spin–orbit interaction, are shown by light green shading. All data are normalized to a current density of 10^5 Acm^{-2} (From Ref. [173]. Copyright © 2014, Rights Managed by Nature Publishing Group)

Figure 26b plots the frequency dependence of the resonance field H_{res}. The FMR linewidth $(\Delta H = \Delta H_{inhomo} + \alpha\omega/\gamma)$ describes the damping in the ferromagnetic system. The broadband nature of the setup allows to determine the inhomogeneous contribution to the damping (Fig. 26c), and the Gilbert damping constant α (Fig. 26d) presents the data from an in-plane scan of the magnetic field, showing that there is a strong uniaxial anisotropy perpendicular to the bar direction. By analyzing the peak positions (Fig. 26e), the SOT-FMR allows to quantify the anisotropy fields in the studied micro- or nanoscale magnet.

Studies of the SOT in (Ga,Mn)As have also identified an additional anti-damping SOT contribution which has a common microscopic origin with the intrinsic anomalous and spin-Hall effects [173]. Unlike the above scattering-related field-like SOT, described within the semiclassical Boltzmann theory, the presence of an anti-damping SOT with a scattering-independent origin is captured by the time-dependent quantum-mechanical perturbation theory. Here the linear-response theory considers the equilibrium distribution function, and the applied electric field perturbs the carrier wave functions.

The anti-damping like SOT with the theoretically predicted symmetries was identified in measurements in (Ga,Mn)As, as shown in Fig. 27 [173]. The all-electrical broadband SOT-FMR technique [46] was applied which allowed to perform 3D vector magnetometry on the driving SOT fields and showed that the anti-damping SOT plays an important role in driving the magnetization dynamics in (Ga,Mn)As.

Magnonic Charge Pumping

In the STT, spin-angular momentum is transferred from the carriers to the magnet where it excites magnetization dynamics. A reciprocal effect to the STT is the spin pumping in which pure spin current is generated from magnetization precession [174, 175]. Spin pumping can be used not only for probing magnetization dynamics in ferromagnets but also spin physics in paramagnets, e.g., for measuring the SHE angles. Magnetization dynamics also produces electrical signals in the ferromagnetic layer through galvanomagnetic effects. Experiments in a (Ga,Mn)As/p-GaAs model system, where sizable galvanomagnetic effects are present, have demonstrated that neglecting the galvanomagnetic effects in the ferromagnet can lead to a large overestimate of the SHE angle in the paramagnet. The study has also shown a method to separate voltages of these different origins in the spin-pumping experiments in the ferromagnet/paramagnet bilayers [151].

The Onsager reciprocity relations imply that there is also a reciprocal phenomenon of the SOT in which electrical signal is generated from magnetization precession in a uniform, spin–orbit coupled magnetic system with broken space inversion symmetry (see Fig. 28) [176, 177]. In this reciprocal SOT effect, no secondary spin–charge conversion element is required, and, as for the SOT, (Ga, Mn)As with broken inversion symmetry in its bulk crystal structure and strong spin–orbit coupled holes represents a favorable model system to explore this phenomenon. The effect was observed in (Ga,Mn)As and was termed a magnonic charge pumping [178].

Light-Induced Torques

Circularly Polarized Light

As discussed in the previous section, current-induced STT is a phenomenon in which angular momentum of a spin-polarized electrical current entering a ferromagnet is transferred to the magnetization. The effect has opened a new research field of electrically driven magnetization dynamics in magnetic nanostructures and plays an important role in the development of a new generation of memory devices and tunable oscillators. Optical excitations of magnetic systems by laser pulses have been a separate research field whose aims are to explore magnetization dynamics at short time scales and enable ultrafast spintronics devices. The observation in (Ga,Mn)As [47] of the optical spin–transfer torque (OSTT) [157, 179] has built the bridge between these two fields of spintronics research. In a pump-and-probe optical experiment, a coherent spin precession in a (Ga,Mn)As ferromagnetic semiconductor was excited by circularly polarized laser pulses. During the pump pulse, the spin-angular momentum of photo-carriers generated by the absorbed light is transferred to the collective magnetization of the ferromagnet.

(Ga,Mn)As is a favorable candidate for observing OSTT [157, 179]. The direct-gap GaAs host allows the generation of a high density of photo-carriers, optical

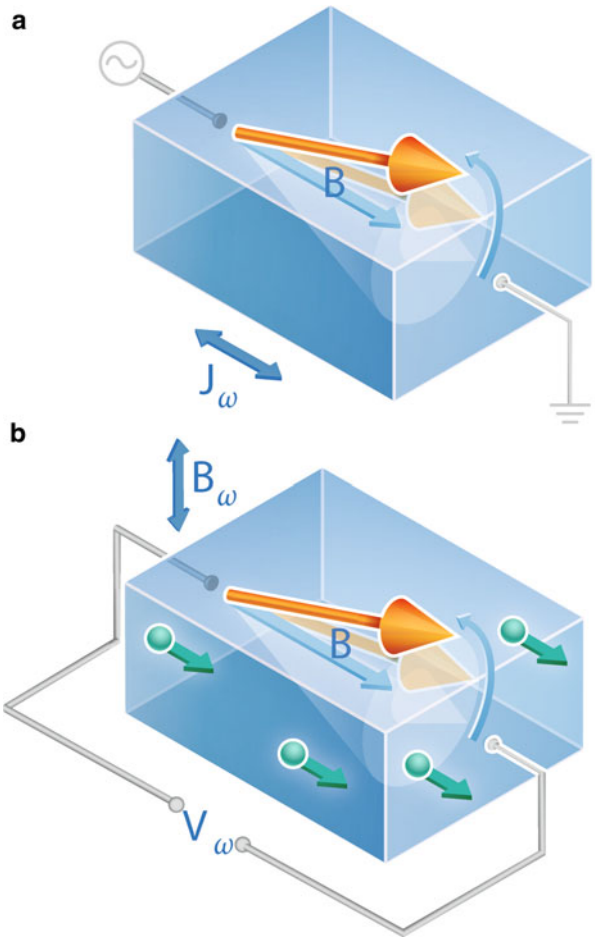

Fig. 28 (**a**) A charge current through (Ga,Mn)As results in a nonequilibrium spin polarization of the carriers, which exchange couples to the magnetization and exerts a torque. The effect is induced by spin–orbit coupling, which mediates the transfer of orbital momentum to spin-angular momentum. An alternating current generates a time-varying torque, which drives magnetic precession resonantly when a magnetic field is applied. (**b**) The reciprocal effect of (**a**). Magnetization precession leads to a nonequilibrium spin concentration, which pumps charge (*green arrows*) and is converted into an alternating charge current by the spin–orbit coupling (Reprinted by permission from Macmillan Publishers Ltd: Nature Nanotechnology [178], copyright (2014))

selection rules for circularly polarized light yield high degree of spin polarization of photo-carriers in the direction of the light propagation, and the carrier spins interact with ferromagnetic moments on Mn via exchange coupling. When the ferromagnetic Mn moments are excited, this can be sensitively detected by probe laser pulses due to strong magneto-optical signals in (Ga,Mn)As [180–189].

Coupled precession dynamics of the magnetization orientation and the nonequilibrium photo-carrier spin density is governed by the analogous equations to Eqs. 8 and 9, where the carrier–Mn moment exchange coupling constant is $J_{ex} \approx 50$ meVnm^3 for holes and $J_{ex} \approx 10$ meVnm^3 for electrons in (Ga,Mn)As. In the optical experiments, P in Eq. 9 is the rate per unit volume at which carrier spins with orientation $\hat{\mathbf{n}}$ are optically injected into the ferromagnet. In the studied experimental geometry with normal incidence of the laser pulse and in-plane easy axis of (Ga,Mn)As, the equilibrium $\hat{\mathbf{M}}$ is perpendicular to $\hat{\mathbf{n}}$. The sign of $\hat{\mathbf{n}}$ is given by the helicity of the circularly polarized laser pulse.

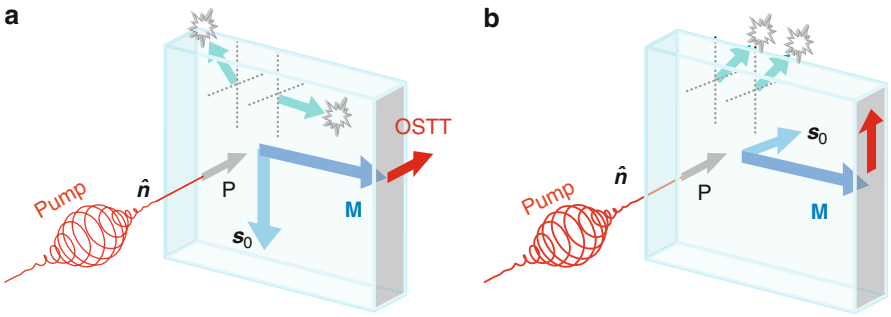

Fig. 29 (**a**) Schematic illustration of the optical spin–transfer torque in the large spin lifetime limit. The rate P of the photo-carrier spin injection along light propagation axis $\hat{\mathbf{n}}$ (normal to the sample plane) is completely transferred to the optical spin–transfer torque (OSTT) acting along the normal to the sample plane on the magnetization $\hat{\mathbf{M}}$ of the ferromagnet. The steady-state component of the injected spin density $\mathbf{s}_0$ is oriented in the plane of the sample and perpendicular to the in-plane equilibrium magnetization vector. The fast precessing component of the spin of a photo-carrier (*small upper arrows*) relaxes to the environment at a random orientation, producing a zero net momentum transfer to the environment. This picture applies to photoelectrons in (Ga,Mn) As. (**b**) A weak torque acting on $\hat{\mathbf{M}}$ produced by photo-carriers with a short spin lifetime. Most of the spin-angular moment is transferred to the environment in this limit. For photo holes in (Ga,Mn) As, this picture is more relevant than the picture of the strong optical spin–transfer torque shown in panel (**a**) (From Ref. [47]. Copyright © 2012, Rights Managed by Nature Publishing Group)

The timescale of photoelectron precession due to the exchange field produced by the high-density ferromagnetic Mn moments is $\tau_{ex} \sim 100$ fs. The major source of spin decoherence of the photoelectrons in (Ga,Mn)As is the exchange interaction with fluctuating Mn moments. Microscopic calculations of the corresponding relaxation time give a typical scale of 10's ps [157]. The other factor that limits τ_s introduced in Eq. 9 is the photoelectron decay time which is also ~10's ps, as inferred from reflectivity measurements of the (Ga,Mn)As samples [47]. Within the spin lifetime, the photoelectron spins therefore precess many times around the exchange field of ferromagnetic moments. In the corresponding regime of $\tau_s \gg \tau_{ex}$, the OSTT has the form of the adiabatic STT given by Eq. 10 and is illustrated in Fig. 29a. The precession time of holes in (Ga,Mn)As is ~10's fs, and the spin lifetime of holes, dominated by the strong spin–orbit coupling, is estimated to ~1–10 f. [157]. Since $\tau_s \lesssim \tau_{ex}$ for holes, their contribution is better approximated by the weaker torque which has the form of nonadiabatic STT given by Eq. 11 and is neglected in the discussion below.

The experimental observation of the magnetization precession in (Ga,Mn)As excited by OSTT, with tire characteristic in opposite phases of the oscillations excited by pump pulses of opposite helicities, is presented in Fig. 30a. In the experiment, the output of a femtosecond laser is divided into a strong, 300 f. long pump pulse and a weak delayed probe pulse that are focused to the same spot on the measured sample. To observe the OSTT, a circularly polarized pump laser beam is used. The pump-induced change of the magneto-optical response of the sample is

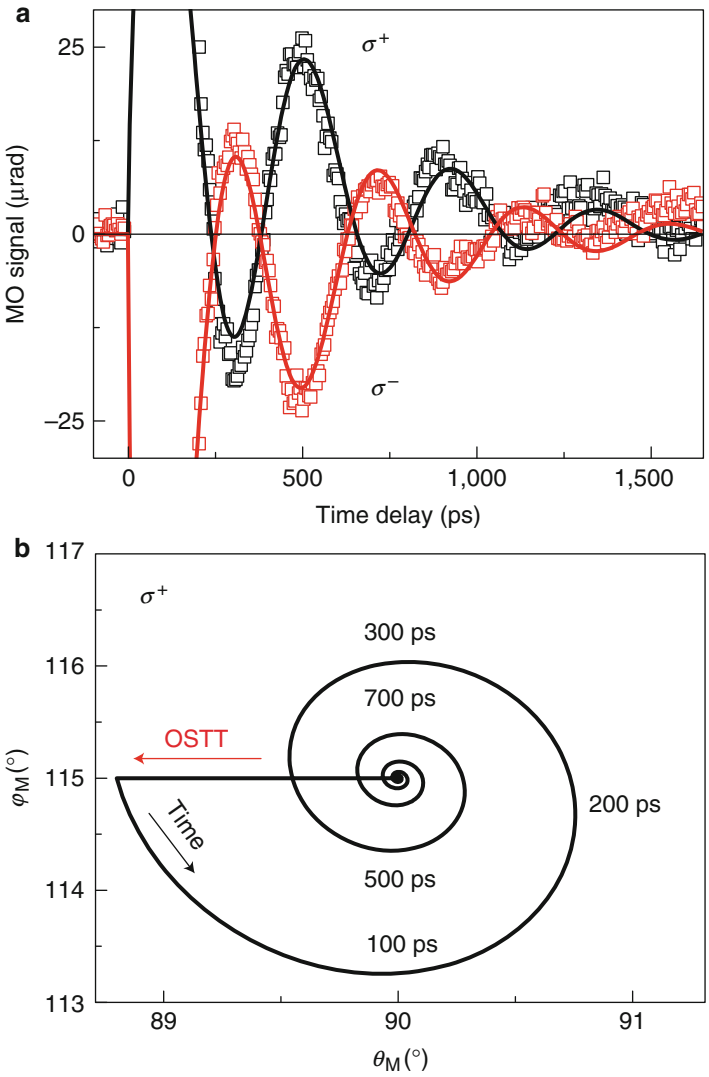

Fig. 30 (**a**) Precession of the magnetization induced in (Ga,Mn)As by σ^+ and σ^- circularly polarized pump pulses. Points are the measured rotations of the polarization plane of the reflected linearly polarized probe pulse as a function of the time delay between pump and probe pulses. *Lines* are the theoretically calculated time-dependent magneto-optical signals. (**b**) The calculated time evolution of the orientation of the magnetization in the sample, described by the polar angle φ_M measured from the [100] axis and the azimuthal angle θ_M measured from the sample normal [001] and induced by the σ^+ circularly polarized pulse. The orientation of the optical spin–transfer torque for σ^+ polarization is shown in the figure by *red arrow* (OSTT). For σ^+ polarization of the pump pulse, the torque points in the opposite direction (From Ref. [47]. Copyright © 2012, Rights Managed by Nature Publishing Group)

measured by a time-delayed linearly polarized probe pulse. The magneto-optical signals shown in Fig. 30a represent the rotation of the polarization plane of the reflected probe beam. Figure 30b shows the calculated time evolution of the polar angle φ_M and the azimuthal angle θ_M of the magnetization corresponding to the measured data in Fig. 30a for the σ^+ helicity.

Since the period of the oscillations seen in Fig. 30 is much larger than tine pump-pulse duration, the action of OSTT is reflected only in the initial phase and amplitude of the free precession of the magnetization. The opposite phase of the measured magneto-optical signals triggered by pump pulses with opposite helicities highlights that the OSTT is not accompanied by any polarization-independent excitation mechanism. Indeed, a linearly polarized pump pulse with any orientation of the polarization is not exciting the magnetization precession. Polarization-independent excitations of magnetization precession in (Ga,Mn)As have been reported prior to the discovery of OSTT [180–189]. The experiments were interpreted in terms of changes of the magnetocrystalline anisotropy induced by the laser pulse [180–189]. The samples studied in Fig. 30a could be also excited by the magnetic anisotropy-related mechanism. In the measurements shown in Fig. 30a, this mechanism was intentionally suppressed in order to highlight the observation of OSTT. This was done by attaching a piezostressor to the (Ga,Mn)As sample which modifies the magnetic anisotropy of the ferromagnetic film due to the differential thermal contraction and allows for an additional in situ electrical control of the in-plane magnetocrystalline anisotropy.

Spin-polarized photo-carriers were also demonstrated to exert an OSTT on the DWs [190]. The resulting optical manipulation of the position of DWs was observed in a perpendicularly magnetized ferromagnetic semiconductor (Ga,Mn)(As,P). The direction of the domain-wall motion was controlled via the OSTT using the helicity of the laser, as illustrated in Fig. 31. Unlike current- or magnetic-field-driven DWs, the OSTT mechanism provides an optical tweezer-like ability to position and locally probe domain walls and to study DW dynamics on ultrashort timescales.

Linearly Polarized Light

As discussed in section "Uniform Magnets," carriers in a magnet under applied electric field can develop a nonequilibrium spin polarization due to the relativistic spin–orbit coupling even in the absence of an external polarizer. This results in the current-induced SOT acting on the magnetization. In this section we review the observation of the optical counterpart of SOT in (Ga,Mn)As [48].

In OSTT discussed above, the external source for injecting spin-polarized carriers is provided by circularly polarized light at normal incidence which yields high degree of out-of-plane spin polarization of injected photo-carriers due to the optical selection rules in GaAs. Since large OSTT requires large spin lifetime of

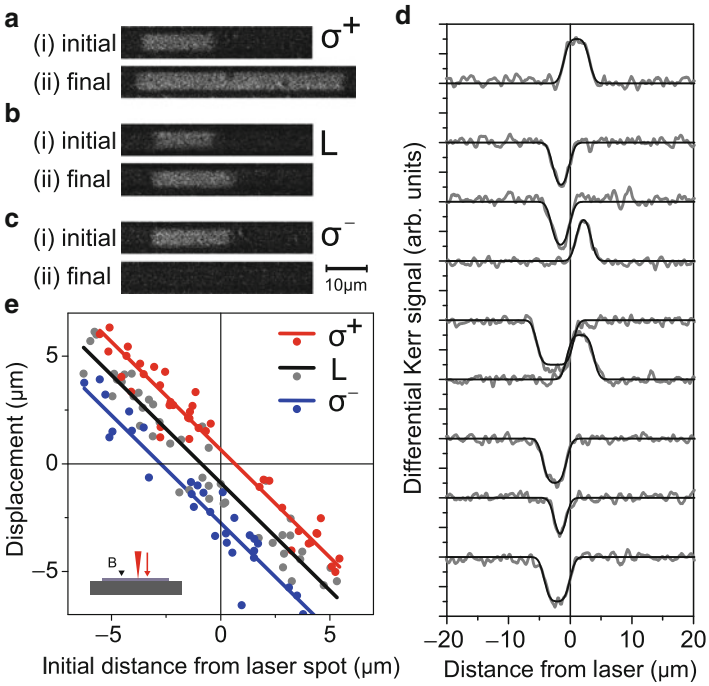

Fig. 31 (**a**), (**b**), and (**c**) Images of the initial domain nucleated by the nucleation pulse and the final domain after illumination by many trains of low-power pulses, as described in the main text. Following nucleation, many measurements of the laser-induced displacement of the right-hand DW are made. For each measurement, the laser is randomly repositioned within 4 μm of the DW and illuminated by a train of ps pulses, below the threshold for domain nucleation. Following the application of many (>50) pulse trains, the DW has moved to the right (*left*) for $\sigma^{\pm}$ polarization and remains relatively unchanged for linear polarization. (**d**) Examples of the change in the magnetic domain following excitation with a linearly polarized pulse for different initial positions of the DW with respect to the laser. A cross section of the difference between the Kerr images taken before and after the laser exposure is plotted against the position relative to the center of the laser spot. Positive (*negative*) signal indicates a shrinking (*growing*) domain. In most cases, the final position indicated by the positive gradient is close to the center of the laser spot, regardless of initial position. (**e**) Plot of the DW displacement versus initial position. The effect of the pulse train is to move the DW to a stationary position, ×0, that is shifted to the right (*left*) for $\sigma^{\pm}$ polarizations, respectively. (*Inset*) A positive B field is defined parallel to the optical axis (From Ref. [190]. Reprinted with permission from A. J. Ramsay et al., Physical Review Letters, 114, 2015. Copyright (2015) by the American Physical Society)

injected carriers, i.e., spin–orbit coupling is detrimental for OSTT, the weakly spin–orbit coupled photoelectrons play the key role in this case. In OSOT, on the other hand, the absence of an external polarizer corresponds to photo-carrier excitations which are independent of the polarization of the pump laser pulses. Since the phenomenon relies on spin–orbit coupling, the nonequilibrium photo holes are essential in this case. Because of the lack of external polarizer and because of strong spin–orbit coupling, precession of carriers in the exchange field of

magnetic moments is not the origin of the torque in this case, in close analogy to the current-induced SOT and reminiscent of the nonadiabatic STT.

The model physical picture of the OSOT is as follows: The optically injected photo holes relax toward the hole Fermi energy of the p-type (Ga,Mn)As on a short (~100 fs) timescale, creating a nonequilibrium excess hole density in the valence band. The change in the occupation of the hole states, as compared to the equilibrium state in dark, and the spin–orbit coupling can generate a nonequilibrium hole spin polarization which is misaligned with the equilibrium orientation of Mn moments. This nonequilibrium photo-hole polarization persists over the timescale of the hole recombination (~ps) during which it exerts a torque on the Mn local moments via the kinetic-exchange coupling. The three key characteristic features, i.e., the nonequilibrium occupation of carrier states, spin–orbit coupling in carrier bands, and the resulting nonequilibrium carrier polarization acting on the magnetic moments via exchange coupling, make OSOT the direct optical counterpart of the current-induced SOT. Since the applied electrical drift (and relaxation) yields a nonequilibrium carrier occupation in the form of asymmetric redistribution on the Fermi surface, the current-induced SOT is observed in systems with broken inversion symmetry in the crystal. OSOT is caused by optical generation (and relaxation) of photo-carriers without an applied drift, and, therefore, the broken inversion symmetry in the crystal is not required. It is replaced by the broken time reversal symmetry, i.e., by a nonzero spin polarization of carrier bands in equilibrium. This is another reason why holes in the strong exchange-split valence band in (Ga,Mn)As govern OSOT.

The schematic illustration and the experimental observation of OSOT are shown in Fig. 32. Apart from the physically more intriguing nature of relativistic OSOT, as compared to OSTT, its experimental identification is complicated by the presence of thermal excitation mechanisms of magnetization dynamics in the case of pump-polarization-independent signals [191, 192]. The absorption of the pump laser pulse leads to photo-injection of electron–hole pairs. The non-radiative recombination of photoelectrons produces a transient increase of lattice temperature which builds up on the timescale of ~ 10 ps and persists over ~ 1000 ps. This results in a quasi-equilibrium easy-axis orientation which is tilted from the equilibrium easy axis. Consequently, Mn moments in (Ga,Mn)As start to precess around quasi-equilibrium easy axis, as illustrated in Fig. 32a, with a typical precession time of ~ 100 ps given by the magnetic anisotropy fields in (Ga,Mn)As. The easy axis stays in-plane and the sense of rotation within the plane of the (Ga,Mn)As film with increasing temperature is uniquely defined. In the notation introduced in Fig. 32c, the change of the in-plane angle $\delta\varphi$ of magnetization during the thermally excited precession can be only positive.

OSOT, illustrated in Fig. 32b, acts during the laser pulse (with a duration of 200 fs) and fades away within the hole recombination time (~ ps). It causes an impulse tilt of the magnetization which allows one to clearly distinguish OSOT from the considerably slower thermal excitation mechanism. Moreover, the initial OSOT-induced tilt of magnetization can yield precession angles that are inaccessible in the thermally induced magnetization dynamics. This provides another

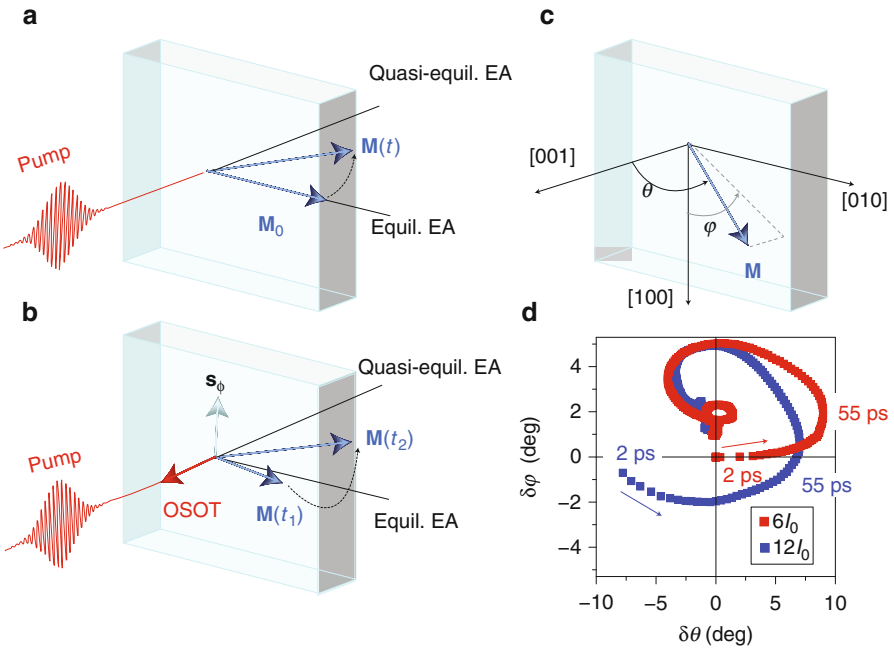

Fig. 32 (**a**) Schematic illustration of the thermally excited precession of magnetization **M**(t) around the transient quasi-equilibrium easy axis (EA). $\mathbf{M}_0$ is the magnetization vector aligned with in-plane equilibrium EA before the pump pulse. (**b**) Schematic illustration of OSOT induced by the in-plane transverse component $\mathbf{s}_{\varphi}$ of the nonequilibrium hole spin polarization. On the timescale of magnetization precession, OSOT causes an instantaneous tilt of the magnetization $\mathbf{M}(t_1)$ which allows to clearly distinguish OSOT from the considerably slower thermal excitation mechanism. The initial OSOT-induced tilt of magnetization can yield precession angles that are inaccessible in the thermally induced magnetization dynamics. (**c**) Definition of the coordinate system. (**d**) Time evolution of the magnetization vector measured in a (Ga,Mn)As material with nominal Mn doping $x = 3$ %. The direction of the time increase is depicted by *arrows*. Magnetization tilt angles $\delta\varphi$ and $\delta\theta$ are measured with respect to equilibrium EA (From Ref. [48].)

evidence for OSOT. Examples of the direct observation of the thermally governed excitation of magnetization at a lower pump-pulse intensity and of the OSOT-governed excitation at a higher intensity are shown in Fig. 32d. These dynamical magneto-optical signals are completely independent of the polarization of pump pulses, i.e., they are the same for any orientation of the polarization plane of linearly polarized pump laser pulses. The distinct features of OSOT, described in the previous paragraph, are clearly visible when comparing the two measured trajectories of magnetization angles.

A full quantitative theory of OSOT is a challenging problem compared to the theory of OSTT [47, 157, 179]. In the latter case, the nonequilibrium spin density of weakly spin–orbit coupled photoelectrons, producing the OSTT, is directly determined by the external polarizer, i.e., by the intensity, propagation axis, and helicity

of the circularly polarized pump laser beam. The relation between the nonequilibrium density of photo holes and the transverse component of their spin polarization, producing OSOT in the case of light-polarization-independent excitations, results from a more complex interplay of spin–orbit coupling and photogeneration and relaxation processes in the spin–split valence band of the ferromagnetic semiconductor [193]. The effective field due to the nonequilibrium spin density of the photo holes, $J_{ex}\mathbf{s}$, generating OSOT can be related in a simplified picture [48] to the hole-density-dependent magnetocrystalline anisotropy field. This can be illustrated using the model kinetic-exchange Hamiltonian $H = H_{host} + J_{ex}cS\hat{\mathbf{M}} \cdot \boldsymbol{\sigma}$ [51, 94], where H_{host} is the host Hamiltonian semiconductor and $\boldsymbol{\sigma}$ is the hole spin operator. The anisotropy field can then be written as [164]

$$\begin{aligned}\mathbf{H}_{an} &= -\frac{1}{cS}\frac{\partial}{\partial\hat{\mathbf{M}}}\sum_a \int d\mathbf{k}\epsilon_{a,\mathbf{k}} f_{a,\mathbf{k}} \\ &= -\frac{1}{cS}\sum_a \int d\mathbf{k}\left\langle a,\mathbf{k}\left|\frac{\partial H}{\partial\hat{\mathbf{M}}}\right|a,\mathbf{k}\right\rangle f_{a,\mathbf{k}} \\ &= -\sum_a \int d\mathbf{k}\langle a,\mathbf{k}|J_{ex}\boldsymbol{\sigma}|a,\mathbf{k}\rangle f_{a,\mathbf{k}} \\ &= -J_{ex}\mathbf{s}\end{aligned} \tag{12}$$

Here $\epsilon_{a,\mathbf{k}}$ and $f_{a,\mathbf{k}}$ are the eigenenergy of H and Fermi distribution function, respectively, labeled by the band and wave vector index. Since the easy-axis orientation is sensitive to the hole density, $\mathbf{H}_{an}$ and the corresponding OSOT field $J_{ex}\mathbf{s}$ can change when the hole density is increased by, e.g., the photoexcitation.

Summary

We have reviewed the electronic and magnetic properties of (III,Mn)V ferromagnetic semiconductors and devices fabricated in these materials, focusing on the most extensively explored and exploited (Ga,Mn)As. Over the two decades of research in (Ga,Mn)As, its material properties have been extensively debated from the basic physics perspective in order to elucidate the role of the high density of magnetic and electrical Mn impurities in the semiconductor host and the implications of the Mn doping on the Curie temperature, conductivity, and other hybrid magneto-semiconducting characteristics of the material. This material research side of (Ga,Mn)As now seems to have reached a rather mature stage. Where (Ga,Mn)As and the related (III,Mn)V materials continue to bring new surprises and inspiration is primarily in the research of relativistic spintronics phenomena and device functionalities. A number of effects that continuously expand the portfolio of spintronics fundamentals have been initially observed in (Ga,Mn)As and subsequently rediscovered or transferred to other magnetic systems, including high Curie temperature ferromagnets relevant for applications. This trend is likely to continue in the future since (Ga,Mn)As encompasses a range of unique and favorable

structural, magnetic, electronic, and optical properties rendering this ferromagnetic semiconductor an ideal model system for research in spintronics phenomena and devices.

Acknowledgments This review is based on numerous helpful discussions with our colleagues. In particular we acknowledge discussions with Richard Campion, Tomasz Dietl, Kevin Edmonds, Andrew Ferguson,Tom Foxon, Bryan Gallagher, Allan MacDonald, Jan Mašek, Petr Němec, Vít Novák, Hideo Ohno, Kamil Olejník, Andrev Rushforth, Jairo Sinova, Karel Výborný, Dieter Weiss, Jorg Wunderlich, and Jan Zemen. We also acknowledge support from the ERC Advanced Grant No. 268066, from the Ministry of Education of the Czech Republic Grant No. LM2011026, and from the Czech Science Foundation Grant No. 14-37427G

References

1. Ohno H, Munekata H, Penney T, von Molnár S, Chang LL (1992) Magnetotransport properties of p-type (In, Mn)As diluted magnetic III-V semiconductors. Phys Rev Lett 68:2664
2. Munekata H, Zaslavsky A, Fumagalli P, Gambino RJ (1993) Preparation of (In, Mn)As/(Ga, Al)Sb magnetic semiconductor heterostructures and their ferromagnetic characteristics. Appl Phys Lett 63:2929
3. Ohno H, Shen A, Matsukura F, Oiwa A, Endo A, Katsumoto S, Iye Y (1996) (Ga,Mn)As: a new diluted magnetic semiconductor based on GaAs. Appl Phys Lett 69:363
4. Hayashi T, Tanaka M, Seto K, Nishinaga T, Ando K (1997) III-V based magnetic(GaMnAs)/nonmagnetic(AlAs) semiconductor superlattices. Appl Phys Lett 71:1825
5. Van Esch A, Van Bockstal L, De Boeck J, Verbanck G, Van Steenbergen AS, Wellmann PJ, Grietens B, Herlach RBF, Borghs G (1997) Interplay between the magnetic and transport properties in the III-V diluted magnetic semiconductor $Ga_{1-x}Mn_xAs$. Phys Rev B 56:13103
6. Ohno H (1998) Making nonmagnetic semiconductors magnetic. Science 281:951
7. Ohno H, Chiba D, Matsukura F, Omiya T, Abe E, Dietl T, Ohno Y, Ohtani K (2000) Electric-field control of ferromagnetism. Nature 408:944
8. Chiba D, Yamanouchi M, Matsukura F, Ohno H (2003) Electrical manipulation of magnetization reversal in a ferromagnetic semiconductor. Science 301:943
9. Chiba D, Matsukura F, Ohno H (2006) Electric-field control of ferromagnetism in (ga, mn)as. Appl Phys Lett 89:162505
10. Wunderlich J, Jungwirth T, Irvine AC, Kaestner B, Shick AB, Campion RP, Williams DA, Gallagher BL (2007) Coulomb blockade anisotropic magnetoresistance and voltage controlled magnetic switching in a ferromagnetic GaMnAs single electron transistor. J Magn Magn Mater 310:1883
11. Chiba D, Sawicki M, Nishitani Y, Nakatani Y, Matsukura F, Ohno H (2008) Magnetization vector manipulation by electric fields. Nature 455:515
12. Olejník K, Owen MHS, Novák V, Mašek J, Irvine AC, Wunderlich J, Jungwirth T (2008) Enhanced annealing, high Curie temperature and low-voltage gating in (Ga,Mn)As: a surface oxide control study. Phys Rev B 78:054403. arXiv:0802.2080
13. Owen MHS, Wunderlich J, Novák V, Olejník K, Zemen J, Výabornaý K, Ogawa S, Irvine AC, Ferguson AJ, Sirringhaus H, Jungwirth T (2009) Low voltage control of ferromagnetism in a semiconductor p-n junction. New J Phys 11:023008. arXiv:0807.0906
14. Stolichnov I, Riester SWE, Trodahl HJ, Setter N, Rushforth AW, Edmonds KW, Campion RP, Foxon CT, Gallagher BL, Jungwirth T (2008) Nonvolatile ferroelectric control of ferromagnetism in (Ga,Mn)As. Nat Mater 7:464. arXiv:0802.2074

15. Riester SWE, Stolichnov I, Trodahl HJ, Setter N, Rushforth AW, Edmonds KW, Campion RP, Foxon CT, Gallagher BL, Jungwirth T (2009) Toward a low-voltage multiferroic transistor: magnetic (ga, mn)as under ferroelectric control. Appl Phys Lett 94:063504
16. Sawicki M, Chiba D, Korbecka A, Nishitani Y, Majewski JA, Matsukura F, Dietl T, Ohno H (2010) Experimental probing of the interplay between ferromagnetism and localisation in (ga, mn)as. Nat Phys 6:22. arXiv:0909.3694
17. Munekata H, Abe T, Koshihara S, Oiwa A, Hirasawa M, Katsumoto S, Iye Y, Urano C, Takagi H (1997) Light-induced ferromagnetism in III-V-based diluted magnetic semiconductor heterostructures. Appl Phys Lett 81:4862
18. Koshihara S, Oiwa A, Hirasawa M, Katsumoto S, Iye Y, Urano C, Takagi H, Munekata H (1997) Ferromagnetic order induced by photogenerated carriers in magnetic III-V semiconductor heterostructures of (In, Mn)As/GaSb. Phys Rev Lett 78:4617
19. Ohno Y, Young DK, Beschoten B, Matsukura F, Ohno H, Awschalom DD (1999) Electrical spin injection in a ferromagnetic semiconductor heterostructure. Nature 402:790
20. Tanaka M, Higo Y (2001) Large tunneling magnetoresistance in GaMnAs/AlAs/GaMnAs ferromagnetic semiconductor tunnel junctions. Phys Rev Lett 87:026602
21. Chiba D, Matsukura F, Ohno H (2004) Tunneling magnetoresistance in (Ga, Mn)As-based heterostructures with a GaAs barrier. Physica E 21:966
22. Saito H, Yuasa S, Ando K (2005) Origin of the tunnel anisotropic magnetoresistance in $Ga_{1-x}Mn_x$ As/ZnSe/$Ga_{1-x}Mn_x$As magnetic tunnel junctions of II-VI/III-V heterostructures. Phys Rev Lett 95:086604
23. Mattana R, Elsen M, George JM, Jaffrès H, Dau FNV, Fert A, Wyczisk MF, Olivier J, Galtier P, Lépine B, Guivarc'h A, Jézéquel G (2005) Chemical profile and magnetoresistance of Ga_{1-x} Mn_x As/GaAs/AlAs/GaAs/$Ga_{1-x}Mn_x$As tunnel junctions. Phys Rev B 71:075206
24. Chiba D, Sato Y, Kita T, Matsukura F, Ohno H (2004) Current-driven magnetization reversal in a ferromagnetic semiconductor (ga,mn)as/gaas/(ga,mn)as tunnel junction. Phys Rev Lett 93:216602. arXiv:cond-mat/0403500
25. Yamanouchi M, Chiba D, Matsukura F, Ohno H (2004) Current-induced domain-wall switching in a ferromagnetic semiconductor structure. Nature 428:539
26. Yamanouchi M, Chiba D, Matsukura F, Dietl T, Ohno H (2006) Velocity of domain-wall motion induced by electrical current in a ferromagnetic semiconductor (Ga,Mn)As. Phys Rev Lett 96:096601. arXiv:cond-mat/0601515
27. Wunderlich J, Irvine AC, Zemen J, Holý V, Rushforth AW, Ranieri ED, Rana U, Výborný K, Sinova J, Foxon CT, Campion RP, Williams DA, Gallagher BL, Jungwirth T (2007) Local control of magnetocrystalline anisotropy in (Ga,Mn)As microdevices: demonstration in current-induced switching. Phys Rev B 76:054424. arXiv:0707.3329
28. Adam J, Vernier N, Ferre J, Thiaville A, Jeudy V, Lemaitre A, Thevenard L, Faini G (2009) Nonadiabatic spin-transfer torque in (Ga, Mn)As with perpendicular anisotropy. Phys Rev B 80:193204
29. Wang KY, Edmonds KW, Irvine AC, Tatara G, Ranieri ED, Wunderlich J, Olejnik K, Rushforth AW, Campion RP, Williams DA, Foxon CT, Gallagher BL (2010) Current-driven domain wall motion across a wide temperature range in a (Ga, Mn)(As, P) device. Appl Phys Lett 97:262102
30. Curiale J, Lemaitre A, Ulysse C, Faini G, Jeudy V (2012) Spin drift velocity, polarization, and current-driven domain-wall motion in (Ga, Mn)(As, P). Phys Rev Lett 108:076604
31. De Ranieri E, Roy PE, Fang D, Vehsthedt EK, Irvine AC, Heiss D, Casiraghi A, Campion RP, Gallagher BL, Jungwirth T, Wunderlich J (2013) Piezo-electric control of the mobility of a domain wall driven by adiabatic and non-adiabatic torques. Nat Mater 12:808
32. Sinova J, Jungwirth T, Liu X, Sasaki Y, Furdyna JK, Atkinson WA, MacDonald AH (2004) Magnetization relaxation in (Ga,Mn)As ferromagnetic semiconductors. Phys Rev B 69:085209. arXiv:cond-mat/0308386
33. Garate I, Gilmore K, Stiles MD, MacDonald AH (2009) Non-adiabatic spin transfer torque in real materials. Phys Rev B 79:104416. arXiv:0812.2570

34. Hals KMD, Nguyen AK, Brataas A (2009) Intrinsic coupling between current and domain wall motion in (ga,mn)as. Phys Rev Lett 102:256601. arXiv:0811.2235
35. Wenisch J, Gould C, Ebel L, Storz J, Pappert K, Schmidt MJ, Kumpf C, Schmidt G, Brunner K, Molenkamp LW (2007) Control of magnetic anisotropy in (Ga,Mn)As by lithography-induced strain relaxation. Phys Rev Lett 99:077201. arXiv:cond-mat/0701479
36. Rushforth AW, Ranieri ED, Zemen J, Wunderlich J, Edmonds KW, King CS, Ahmad E, Campion RP, Foxon CT, Gallagher BL, Výborný K, Kučera J, Jungwirth T (2008) Voltage control of magnetocrystalline anisotropy in ferromagnetic - semiconductor/piezoelectric hybrid structures. Phys Rev B 78:085314. arXiv:0801.0886
37. Overby M, Chernyshov A, Rokhinson LP, Liu X, Furdyna JK (2008) GaMnAs-based hybrid multiferroic memory device. Appl Phys Lett 92:192501. arXiv:0801.4191
38. Goennenwein STB, Althammer M, Bihler C, Brandlmaier A, Geprägs S, Opel M, Schoch W, Limmer W, Gross R, Brandt MS (2008) Piezo-voltage control of magnetization orientation in a ferromagnetic semiconductor. Phys Status Solidi (RRL) 2:96
39. Gould C, Rüster C, Jungwirth T, Girgis E, Schott GM, Giraud R, Brunner K, Schmidt G, Molenkamp LW (2004) Tunneling anisotropic magnetoresistance: a spin-valve like tunnel magnetoresistance using a single magnetic layer. Phys Rev Lett 93:117203. arXiv:cond-mat/0407735
40. Moser J, Matos-Abiague A, Schuh D, Wegscheider W, Fabian J, Weiss D (2007) Tunneling anisotropic magnetoresistance and spin-orbit coupling in fe/gaas/au tunnel junctions. Phys Rev Lett 99:056601. arXiv:cond-mat/0611406
41. Park BG, Wunderlich J, Marti X, Holy V, Kurosaki Y, Yamada M, Yamamoto H, Nishide A, Hayakawa J, Takahashi H, Shick AB, Jung-wirth T (2011) A spin-valve-like magnetoresistance of an antiferromagnet-based tunnel junction. Nat Mater 10:347. arXiv:1011.3188
42. Wunderlich J, Jungwirth T, Kaestner B, Irvine AC, Wang KY, Stone N, Rana U, Giddings AD, Shick AB, Foxon CT, Campion RP, Williams DA, Gallagher BL (2006) Coulomb blockade anisotropic magnetoresistance effect in a (Ga,Mn)As single-electron transistor. Phys Rev Lett 97:077201. arXiv:cond-mat/0602608
43. Bernand-Mantel A, Seneor P, Bouzehouane K, Fusil S, Deranlot C, Petroff F, Fert A (2009) Anisotropic magneto-coulomb effects and magnetic single-electron-transistor action in a single nanoparticle. Nat Phys 5:920
44. Ciccarelli C, Zarbo LP, Irvine AC, Campion RP, Gallagher BL, Wunderlich J, Jungwirth T, Ferguson AJ (2012) Spin gating electrical current. Appl Phys Lett 101:122411. arXiv:1203.2439
45. Chernyshov A, Overby M, Liu X, Furdyna JK, Lyanda-Geller Y, Rokhinson LP (2009) Evidence for reversible control of magnetization in a ferromagnetic material by means of spin-orbit magnetic field. Nat Phys 5:656. arXiv:0812.3160
46. Fang D, Kurebayashi H, Wunderlich J, Vyborny K, Zarbo LP, Campion RP, Casiraghi A, Gallagher BL, Jungwirth T, Ferguson AJ (2011) Spin-orbit driven ferromagnetic resonance: a nanoscale magnetic characterisation technique. Nat Nanotechnol 6:413. arXiv:1012.2397
47. Nemec P, Rozkotova E, Tesarova N, Trojanek F, Ranieri ED, Olejnik K, Zemen J, Novak V, Cukr M, Maly P, Jungwirth T (2012) Experimental observation of the optical spin transfer torque. Nat Phys 8:411. arXiv:1201.1436
48. Tesarova N, Nemec P, Rozkotova E, Zemen J, Trojanek F, Olejnik K, Novak V, Maly P, Jungwirth T (2013) Experimental observation of the optical spin-orbit torque. Nat Photonics 7:492. arXiv:1207.0307
49. Matsukura F, Ohno H, Dietl T (2002) In: Buschow KHJ (ed) Handbook of magnetic materials, vol 14. Elsevier, Amsterdam, p 1. From Ohno Lab Homepage
50. Dietl T (2003) In: Kramer B (ed) Advances in solid state physics. Springer, Berlin, p 413. arXiv:cond-mat/0306479
51. Jungwirth T, Sinova J, Mašek J, Kučera J, MacDonald AH (2006) Theory of ferromagnetic (III,Mn)V semiconductors. Rev Mod Phys 78:809. arXiv:cond-mat/0603380

52. Sato K, Bergqvist L, Kudrnovský J, Dederichs PH, Eriksson O, Turek I, Sanyal B, Bouzerar G, Katayama-Yoshida H, Dinh VA, Fukushima T, Kizaki H, Zeller R (2010) First-principles theory of dilute magnetic semiconductors. Rev Mod Phys 82:1633
53. Dietl T, Ohno H (2014) Dilute ferromagnetic semiconductors: physics and spintronic structures. Rev Mod Phys 86:187. arXiv:1307.3429
54. Jungwirth T, Wunderlich J, Novak V, Olejnik K, Gallagher BL, Campion RP, Edmonds KW, Rushforth AW, Ferguson AJ, Nemec P (2014) Spin-dependent phenomena and device concepts explored in (Ga,Mn)As. Rev Mod Phys 86:855. arXiv:1310.1944
55. Chapman RA, Hutchinson WG (1967) Photoexcitation and photoionization of neutral manganese acceptors in gallium arsenide. Phys Rev Lett 18:443
56. Blakemore JS, Brown WJ, Stass ML, Woodbury DA (1973) Thermal activation energy of manganese acceptors in gallium arsenide as a function of impurity spacing. J Appl Phys 44:3352
57. Bhattacharjee AK, à la Guillaume CB (2000) Model for the mn acceptor in gaas. Solid State Commun 113:17
58. Yakunin AM, Silov AY, Koenraad PM, Wolter JH, Van Roy W, De Boeck J, Tang JM, Flatté ME (2004) Spatial structure of an individual mn acceptor in gaas. Phys Rev Lett 92:216806. arXiv:cond-mat/0402019
59. Madelung O, Rössler U, Schulz M (2003) Impurities and, defects in group IV elements, IV-IV and III-V compounds. Part b: group IV-IV and III-V compounds. Landolt-Börnstein – group III condensed matter, vol 41A2b. Springer, Berlin/Heidelberg
60. Ohno H (1999) Properties of ferromagnetic iii-v semiconductors. J Magn Magn Mater 200:110
61. Campion RP, Edmonds KW, Zhao LX, Wang KY, Foxon CT, Gallagher BL, Staddon CR (2003) The growth of gamnas films by molecular beam epitaxy using arsenic dimers. J Cryst Growth 251:311
62. Potashnik SJ, Ku KC, Mahendiran R, Chun SH, Wang RF, Samarth N, Schiffer P (2002) Saturated ferromagnetism and magnetization deficit in optimally annealed (Ga,Mn)As epilayers. Phys Rev B 66:012408. arXiv:cond-mat/0204250
63. Jungwirth T, Sinova J, MacDonald AH, Gallagher BL, Novák V, Edmonds KW, Rushforth AW, Campion RP, Foxon CT, Eaves L, Olejník K, Mašek J, Yang SRE, Wunderlich J, Gould C, Molenkamp LW, Dietl T, Ohno H (2007) Character of states near the fermi level in (Ga,Mn)As: impurity to valence band crossover. Phys Rev B 76:125206. arXiv:0707.0665
64. Ruzmetov D, Scherschligt J, Baxter DV, Wojtowicz T, Liu X, Sasaki Y, Furdyna JK, Yu KM, Walukiewicz W (2004) High-temperature hall effect in $Ga_{1-x}Mn_xAs$. Phys Rev B 69:155207
65. MacDonald AH, Schiffer P, Samarth N (2005) Ferromagnetic semiconductors: moving beyond (Ga,Mn)As. Nat Mater 4:195. arXiv:cond-mat/0503185
66. Jungwirth T, Wang KY, Mašek J, Edmonds KW, König J, Sinova J, Polini M, Goncharuk NA, MacDonald AH, Sawicki M, Campion RP, Zhao LX, Foxon CT, Gallagher BL (2005) Prospects for high temperature ferromagnetism in (Ga,Mn)As semiconductors. Phys Rev B 72:165204. arXiv:cond-mat/0505215
67. Shklovskii BI, Efros AL (1984) Electronic properties of doped semiconductors. Springer, New York
68. Lee PA, Ramakrishnan TV (1985) Disordered electronic systems. Rev Mod Phys 57:287
69. Paalanen MA, Bhatt RN (1991) Transport and thermodynamic properties across the metal-insulator transition. Physica B 169:223
70. Dietl T (2007) Origin of ferromagnetic response in diluted magnetic semiconductors and oxides. J Phys Condens Matter 19:165204. arXiv:0711.0340
71. Dietl T (2008) Interplay between carrier localization and magnetism in diluted magnetic and ferromagnetic semiconductors. J Phys Soc Jpn 77:031005. arXiv:0712.1293
72. Ohya S, Takata K, Tanaka M (2011) Nearly nonmagnetic valence band of the ferromagnetic semiconductor GaMnAs. Nat Phys 7:342

73. Gray AX, Minár J, Ueda S, Stone PR, Yamashita Y, Fujii J, Braun J, Plucinski L, Schneider CM, Panaccione G, Ebert H, Dubon OD, Kobayashi K, Fadley CS (2012) Bulk electronic structure of the dilute magnetic semiconductor GaMnAs through hard x-ray angle-resolved photoemission. Nat Mater 11:957
74. Di Marco I, Thunstrom P, Katsnelson MI, Sadowski J, Karlsson K, Lebegue S, Kanski J, Eriksson O (2013) Electron correlations in MnxGa1xAs as seen by resonant electron spectroscopy and dynamical mean field theory. Nat Commun 4:2645
75. Mašek J, Máca F, Kudrnovský J, Makarovsky O, Eaves L, Campion RP, Edmonds KW, Rushforth AW, Foxon CT, Gallagher BL, Novak V, Sinova J, Jungwirth T (2010) Microscopic analysis of the valence band and impurity band theories of (Ga,Mn)As. Phys Rev Lett 105:227202. arXiv:1007.4704
76. Wang M, Edmonds KW, Gallagher BL, Rushforth AW, Makarovsky O, Patane A, Campion RP, Foxon CT, Novak V, Jungwirth T (2013) High curie temperatures at low compensation in the ferromagnetic semiconductor (ga,mn)as. Phys Rev B 87, 121301(R). arXiv:1211.3860
77. Dobrowolska M, Tivakornsasithorn K, Liu X, Furdyna JK, Berciu M, Yu KM, Walukiewicz W (2012) Controlling the Curie temperature in (Ga, Mn)As through location of the fermi level within the impurity band. Nat Mater 11:444
78. Dobrowolska M, Liu X, Furdyna JK, Berciu M, Yu KM, Walukiewicz W (2012) Response to the comment of K. W. Edmonds et al. http://arxiv.org/abs/1211.4051
79. Nemec P, Novak V, Tesarova N, Rozkotova E, Reichlova H, Butkovicova D, Trojanek F, Olejnik K, Maly P, Campion RP, Gallagher BL, Sinova J, Jungwirth T (2013) The essential role of carefully optimized synthesis for elucidating intrinsic material properties of (Ga,Mn)As. Nat Commun 4:1422. arXiv:1207.0310
80. Gao H, Cernov C, Jungwirth T, Sinova J (2015) Disorder and localization effects on the local spectroscopic and infrared-optical properties of GaMnAs. Phys Rev B 91:245201. arXiv:1502.05705v1
81. Richardella A, Roushan P, Mack S, Zhou B, Huse DA, Awschalom DD, Yazdani A (2010) Visualizing critical correlations near the metal-insulator transition in $Ga_{1-x}Mn_xAs$. Science 327:665
82. Yokoyama M, Yamaguchi H, Ogawa T, Tanaka M (2005) Zinc-blende-type mnas nanoclusters embedded in gaas. J Appl Phys 97, 10D317
83. Kovacs A, Sadowski J, Kasama T, Domagala J, Mathieu R, Dietl T, Dunin-Borkowski RE (2011) Voids and mn-rich inclusions in a (ga, mn)as ferromagnetic semiconductor investigated by transmission electron microscopy. J Appl Phys 109:083546
84. Novák V, Olejník K, Wunderlich J, Cukr M, Výborný K, Rushforth AW, Edmonds KW, Campion RP, Gallagher BL, Sinova J, Jungwirth T (2008) Curie point singularity in the temperature derivative of resistivity in (Ga,Mn)As. Phys Rev Lett 101:077201. arXiv:0804.1578
85. Fisher ME, Langer JS (1968) Resistive anomalies at magnetic critical points. Phys Rev Lett 20:665
86. López-Sancho MP, Brey L (2003) Temperature dependence of the dielectric constant and resistivity of diluted magnetic semiconductors. Phys Rev B 68:113201. arXiv:cond-mat/0302237
87. Moca CP, Sheu BL, Samarth N, Schiffer P, Janko B, Zarand G (2009) Scaling theory of magnetoresistance and carrier localization in GaMnAs. Phys Rev Lett 102:137203
88. Jungwirth T, Mašek J, Wang KY, Edmonds KW, Sawicki M, Polini M, Sinova J, MacDonald AH, Campion RP, Zhao LX, Farley NRS, Johal TK, van der Laan G, Foxon CT, Gallagher BL (2006) Low-temperature magnetization of (Ga,Mn)As semiconductors. Phys Rev B 73:165205. arXiv:cond-mat/0508255
89. Máca F, Mašek J (2002) Electronic states in $Ga_{1-x}Mn_xAs$: substitutional versus interstitial position of mn. Phys Rev B 65:235209

90. Yu KM, Walukiewicz W, Wojtowicz T, Kuryliszyn I, Liu X, Sasaki Y, Furdyna JK (2002) Effect of the location of Mn sites in ferromagnetic $Ga_{1-x}Mn_xAs$ on its curie temperature. Phys Rev B 65:201303
91. Edmonds KW, Wang KY, Campion RP, Neumann AC, Farley NRS, Gallagher BL, Foxon CT (2002) High Curie temperature GaM-nAs obtained by resistance-monitored annealing. Appl Phys Lett 81:4991. arXiv:cond-mat/0209554
92. Dietl T, Ohno H, Matsukura F (2001) Hole-mediated ferromagnetism in tetrahedrally coordinated semiconductors. Phys Rev B 63:195205. arXiv:cond-mat/0007190
93. Abolfath M, Jungwirth T, Brum J, MacDonald AH (2001) Theory of magnetic anisotropy in $III_{1-x}Mn_xV$ ferromagnets. Phys Rev B 63:054418. arXiv:cond-mat/0006093
94. Zemen J, Kucera J, Olejnik K, Jungwirth T (2009) Magneto crystalline anisotropies in (Ga, Mn)As: a systematic theoretical study and comparison with experiment. Phys Rev B 80:155203. arXiv:0904.0993
95. König J, Jungwirth T, MacDonald AH (2001) Theory of magnetic properties and spin-wave dispersion for ferromagnetic (Ga,Mn)As. Phys Rev B 64:184423. arXiv:cond-mat/0103116
96. Brey L, Gómez-Santos G (2003) Magnetic properties of GaMnAs from an effective Heisenberg Hamiltonian. Phys Rev B 68:115206. arXiv:cond-mat/0306125
97. Bouzerar G (2007) Magnetic spin excitations in diluted ferromagnetic systems: the case of $Ga_{1-x}Mn_xAs$. Europhys Lett 79:57007. arXiv:cond-mat/0610465
98. Werpachowska A, Dietl T (2010) Theory of spin waves in ferromagnetic (Ga, Mn)As. Phys Rev B 82:085204
99. Baibich MN, Broto JM, Fert A, Nguyen Van Dau F, Petroff F, Etienne P, Creuzet G, Friederich A, Chazelas J (1988) Giant Magnetoresistance of (001)Fe/(001)Cr Magnetic Superlattices. Phys Rev Lett 61:2472–2475
100. McGuire T, Potter R (1975) Anisotropic magnetoresistance in ferromagnetic 3d alloys. IEEE Trans Magn 11:1018–1038
101. Baxter DV, Ruzmetov D, Scherschligt J, Sasaki Y, Liu X, Furdyna JK, Mielke CH (2002) Anisotropic magnetoresistance in $Ga_{1-x}Mn_xAs$. Phys Rev B 65:212407
102. Jungwirth T, Sinova J, Wang KY, Edmonds KW, Campion RP, Gallagher BL, Foxon CT, Niu Q, MacDonald AH (2003) Dc-transport properties of ferromagnetic (ga,mn)as semiconductors. Appl Phys Lett 83:320. arXiv:cond-mat/0302060
103. Tang HX, Kawakami RK, Awschalom DD, Roukes ML (2003) Giant planar hall effect in epitaxial (ga,mn)as devices. Phys Rev Lett 90:107201. arXiv:cond-mat/0210118
104. Matsukura F, Sawicki M, Dietl T, Chiba D, Ohno H (2004) Magnetotransport properties of metallic (ga, mn)as films with compressive and tensile strain. Physica E 21:1032
105. Goennenwein STB, Russo S, Morpurgo AF, Klapwijk TM, Van Roy W, De Boeck J (2005) Quantitative study of magnetotransport through a (ga,mn)as single ferromagnetic domain. Phys Rev B 71:193306. arXiv:cond-mat/0412290
106. Wang KY, Edmonds KW, Campion RP, Zhao LX, Foxon CT, Gallagher BL (2005) Anisotropic magnetoresistance and magnetic anisotropy in high-quality(ga,mn)as films. Phys Rev B 72:085201. arXiv:cond-mat/0506250
107. Limmer W, Glunk M, Daeubler J, Hummel T, Schoch W, Sauer R, Bihler C, Huebl H, Brandt MS, Goennenwein STB (2006) Angle-dependent magnetotransport in cubic and tetragonal ferromagnets: application to (001)-and (113)a-oriented (ga,mn)as. Phys Rev B 74:205205. arXiv:cond-mat/0607679
108. Rushforth AW, Výborný K, King CS, Edmonds KW, Campion RP, Foxon CT, Wunderlich J, Irvine AC, Vašek P, Novák V, Olejník K, Sinova J, Jungwirth T, Gallagher BL (2007) Anisotropic magnetoresistance components in (ga,mn)as. Phys Rev Lett 99:147207. arXiv:cond-mat/0702357
109. Thomson W (1856) On the electro-dynamic qualities of metals: effects of magnetization on the electric conductivity of nickel and of iron. Proc R Soc Lond 8:546
110. Daughton J (1992) Magnetoresistive memory technology. Thin Solid Films 216:162

111. Jungwirth T, Abolfath M, Sinova J, Kučera J, MacDonald AH (2002) Boltzmann theory of engineered anisotropic magnetoresistance in (ga,mn)as. Appl Phys Lett 81:4029. arXiv:cond-mat/0206416
112. Döring W (1938) Die Abhängigkeit des widerstandes von nickelkristallen von der richtung der spontanen magnetisierung. Ann Phys (Leipzig) 424:259
113. Jungwirth T, Niu Q, MacDonald AH (2002) Anomalous Hall effect in ferromagnetic semiconductors. Phys Rev Lett 88:207208. arXiv:cond-mat/0110484
114. Sawicki M, Wang K-Y, Edmonds KW, Campion RP, Staddon CR, Farley NRS, Foxon CT, Papis E, Kaminska E, Piotrowska A, Dietl T, Gallagher BL (2005) In-plane uniaxial anisotropy rotations in (ga,mn)as thin films. Phys Rev B 71:121302. arXiv:cond-mat/0410544
115. Rushforth AW, Giddings AD, Edmonds KW, Campion RP, Foxon CT, Gallagher BL (2006) Amr and magnetometry studies of ultra thin gamnas films. Phys Status Solidi C 3:4078. arXiv:cond-mat/0610692
116. Binasch G, Grünberg P, Saurenbach F, Zinn W (1989) Enhanced magnetoresistance in layered magnetic structures with antiferromagnetic interlayer exchange. Phys Rev B 39:4828
117. Julliere M (1975) Tunneling between ferromagnetic films. Phys Lett A 54:225
118. Moodera JS, Kinder LR, Wong TM, Meservey R (1995) Large magnetoresistance at room temperature in ferromagnetic thin film tunnel junctions. Phys Rev Lett 74:3273
119. Miyazaki T, Tezuka N (1995) Giant magnetic tunneling effect in fe/al2o3/fe junction. J Magn Magn Mater 139:L231
120. Chappert C, Fert A, Dau FNV (2007) The emergence of spin electronics in data storage. Nat Mater 6:813
121. Brey L, Tejedor C, Fernández-Rossier J (2004) Tunnel magneto-resistance in gamnas: going beyond Jullière formula. Appl Phys Lett 85:1996. arXiv:cond-mat/0405473
122. Sankowski P, Kacman P, Majewski JA, Dietl T (2007) Spin-dependent tunneling in modulated structures of (ga,mn)as. Phys Rev B 75:045306. arXiv:cond-mat/0607206
123. Saffarzadeh A, Shokri AA (2006) Quantum theory of tunneling magnetoresistance in gamnas/gaas/gamnas heterostructures. J Magn Magn Mater 305:141. arXiv:cond-mat/0608006
124. Ohya S, Hai PN, Mizuno Y, Tanaka M (2007) Quantum-size effect and tunneling magnetoresistance in ferromagnetic-semiconductor quantum heterostructures. Phys Rev B 75:155328. arXiv:cond-mat/0608357
125. Elsen M, Jaffrès H, Mattana R, Thevenard L, Lemaître A, George JM (2007) Spin-polarized tunneling as a probe of the electronic properties of $Ga_{1-x}Mn_xAs$ heterostructures. Phys Rev B 76:144415. arXiv:0706.0109
126. Rüster C, Gould C, Jungwirth T, Sinova J, Schott GM, Giraud R, Brunner K, Schmidt G, Molenkamp LW (2005) Very large tunneling anisotropic magnetoresistance of a (ga,mn)as/gaas/(ga,mn)as stack. Phys Rev Lett 94:027203. arXiv:cond-mat/0408532
127. Giraud R, Gryglas M, Thevenard L, Lemaître A, Faini G (2005) Voltage-controlled tunneling anisotropic magneto-resistance of a ferromagnetic p++ (ga,mn)as/n+ gaas zener-esaki diode. Appl Phys Lett 87:242505. arXiv:cond-mat/0509065
128. Ciorga M, Einwanger A, Sadowski J, Wegscheider W, Weiss D (2007) Tunneling anisotropic magnetoresistance effect in a p+−(ga, mn)as/n+−gaas esaki diode. Phys Status Solidi A 204:186
129. Rüster C, Gould C, Jungwirth T, Girgis E, Schott GM, Giraud R, Brunner K, Schmidt G, Molenkamp LW (2005) Tunneling anisotropic magnetoresistance: creating a spin-valve-like signal using a single ferromagnetic semiconductor layer. J Appl Phys 97, 10C506
130. Pappert K, Schmidt MJ, Hümpfner S, Rüster C, Schott GM, Brunner K, Gould C, Schmidt G, Molenkamp LW (2006) Magnetization-switched metal-insulator transition in a (ga,mn)as tunnel device. Phys Rev Lett 97:186402. arXiv:cond-mat/0608683
131. Giddings AD, Khalid MN, Jungwirth T, Wunderlich J, Yasin S, Campion RP, Edmonds KW, Sinova J, Ito K, Wang KY, Williams D, Gallagher BL, Foxon CT (2005) Large tunneling

anisotropic magnetoresistance in (ga,mn)as nanoconstrictions. Phys Rev Lett 94:127202. arXiv:cond-mat/0409209
132. Rüster C, Borzenko T, Gould C, Schmidt G, Molenkamp LW, Liu X, Wojtowicz TJ, Furdyna JK, Yu ZG, Flatté ME (2003) Very large magnetoresistance in lateral ferromagnetic (ga,mn) as wires with nanoconstrictions. Phys Rev Lett 91:216602. arXiv:cond-mat/0308385
133. Schlapps M, Doeppe M, Wagner K, Reinwald M, Wegscheider W, Weiss D (2006) Transport through (ga, mn)as nanoconstrictions. Phys Status Solidi A 203:3597
134. Wunderlich J, Jungwirth T, Novák V, Irvine AC, Kaestner B, Shick AB, Foxon CT, Campion RP, Williams DA, Gallagher BL (2007) Ordinary and extraordinary coulomb blockade magnetoresistance in (ga, mn)as single electron transistor. Solid State Commun 144:536
135. Schlapps M, Lermer T, Geissler S, Neumaier D, Sadowski J, Schuh D, Wegscheider W, Weiss D (2009) Transport through (ga,mn)as nanoislands: coulomb blockade and temperature dependence of the conductance. Phys Rev B 80:125330. arXiv:0904.3225
136. Hampton J, Eisenstein J, Pfeiffer L, West K (1995) Capacitance of two-dimensional electron systems subject to an in-plane magnetic field. Solid State Commun 94:559–562
137. Jungwirth T, Smrčka L (1995) Capacitance of gated GaAs/$Al_xGa_{1-x}As$ heterostructures subject to in-plane magnetic field. Phys Rev B 51:10181–10184
138. McCarthy KT, Hebard AF, Arnason SB (2003) Magnetocapacitance: probe of spin-dependent potentials. Phys Rev Lett 90:117201
139. Kaiju H, Fujita S, Morozumi T, Shiiki K (2002) Magnetocapacitance effect of spin tunneling junctions. J Appl Phys 91:7430–7432
140. Padhan P, LeClair P, Gupta A, Tsunekawa K, Djayaprawira DD (2007) Frequency-dependent magnetoresistance and magnetocapacitance properties of magnetic tunnel junctions with MgO tunnel barrier. Appl Phys Lett 90:142105
141. Chang Y-M, Li K-S, Huang H, Tung M-J, Tong S-Y, Lin M-T (2010) Extraction of the tunnel magneto-capacitance with two-terminal measurements. J Appl Phys 107:093904
142. Haigh JA, Ciccarelli C, Betz AC, Irvine A, Novák V, Jungwirth T, Wunderlich J (2015) Anisotropic magnetocapacitance in ferromagnetic-plate capacitors. Phys Rev B 91, 140409(R). doi:10.1103/PhysRevB.91.140409
143. Kopp T, Mannhart J (2009) Calculation of the capacitances of conductors: perspectives for the optimization of electronic devices. J Appl Phys 106:064504
144. Neumaier D, Turek M, Wurstbauer U, Vogl A, Utz M, Wegscheider W, Weiss D (2009) All-electrical measurement of the density of states in (ga, mn)as. Phys Rev Lett 103:087203
145. Ono K, Shimada H, Ootuka Y (1997) Enhanced magnetic valve effect and magneto-coulomb oscillations in ferromagnetic single electron transistor. J Physical Soc Japan 66:1261–1264
146. Ono K, Shimada H, Ootuka Y (1998) Ferromagnetic single electron transistor. Solid State Electron 42:1407–1411
147. Ono K, Shimada H, Ootuka Y (1997) Enhanced magnetic valve effect and magneto-coulomb oscillations in ferromagnetic single electron transistor. J Phys Soc Jpn 66:1261
148. Chappert C, Fert A, Van Dau FN (2007) The emergence of spin electronics in data storage. Nat Mater 6:813–823. http://www.ncbi.nlm.nih.gov/pubmed/17972936
149. Olejník K, Novák V, Wunderlich J, Jungwirth T (2015) Electrical detection of magnetization reversal without auxiliary magnets. Phys Rev B 91:18. doi:10.1103/PhysRevB.91.180402
150. Avci CO, Garello K, Ghosh A, Gabureac M, Alvarado SF, Gambardella P. Unidirectional spin Hall magnetoresistance in ferromagnet/normal metal bilayers. arXiv:1502.06898v1
151. Chen L, Matsukura F, Ohno H (2013) Direct-current voltages in (Ga,Mn)As structures induced by ferromagnetic resonance. Nat Commun 4:2055. http://www.ncbi.nlm.nih.gov/pubmed/23784479
152. Skinner TD, Olejnik K, Cunningham LK, Kurebayashi H, Campion RP, Gallagher BL, Jungwirth T, Ferguson AJ (2015) Complementary spin-Hall and inverse spin-galvanic effect torques in a ferromagnet/semiconductor bilayer. Nat Commun 6:6730
153. Nakayama H, Althammer M, Chen Y-T, Uchida K, Kajiwara Y, Kikuchi D, Ohtani T, Geprägs S, Opel M, Takahashi S, Gross R, Bauer GEW, Goennenwein STB, Saitoh E

(2013) Spin hall magnetoresistance induced by a nonequilibrium proximity effect. Phys Rev Lett 110:206601. doi:10.1103/PhysRevLett.110.206601
154. Ralph D, Stiles M, Bader S (eds) (2008) Current perspectives: spin transfer torques. J Magn Magn Mater 320:1189
155. Zhang S, Li Z (2004) Roles of nonequilibrium conduction electrons on the magnetization dynamics of ferromagnets. Phys Rev Lett 93:127204
156. Vanhaverbeke A, Viret M (2007) Simple model of current-induced spin torque in domain walls. Phys Rev B 75:024411
157. Fernández-Rossier J, Núñez AS, Abolfath M, MacDonald AH (2003) Optical spin transfer in ferromagnetic semiconductors. arXiv:cond-mat/0304492
158. Slonczewski JC (1996) Current-driven excitation of magnetic multilayers. J Magn Magn Mater 159:L1
159. Berger L (1996) Emission of spin waves by a magnetic multilayer traversed by a current. Phys Rev B 54:9353
160. Metaxas PJ, Jamet JP, Mougin A, Cormier M, Ferre J, Baltz V, Rodmacq B, Dieny B, Stamps RL (2007) Creep and flow regimes of magnetic domain-wall motion in ultrathin pt/co/pt films with perpendicular anisotropy. Phys Rev Lett 99:217208
161. Mougin A, Cormier M, Adam JP, Metaxas PJ, Ferre J (2007) Domain wall mobility, stability and walker breakdown in magnetic nanowires. EPL 78:57007
162. Bernevig BA, Vafek O (2005) Piezo-magnetoelectric effects in p-doped semiconductors. Phys Rev B 72:033203
163. Manchon A, Zhang S (2009) Theory of spin torque due to spin-orbit coupling. Phys Rev B 79:094422
164. Garate I, MacDonald AH (2009) Influence of a transport current on magnetic anisotropy in gyrotropic ferromagnets. Phys Rev B 80:134403. arXiv:0905.3856
165. Miron IM, Gaudin G, Auffret S, Rodmacq B, Schuhl A, Pizzini S, Vogel J, Gambardella P (2010) Current-driven spin torque induced by the Rashba effect in a ferromagnetic metal layer. Nat Mater 9:230
166. Gambardella P, Miron IM (2011) Current-induced spin-orbit torques. Phil Trans R Soc A 369:3175
167. Manchon A, Zhang S (2008) Theory of nonequilibrium intrinsic spin torque in a single nanomagnet. Phys Rev B 78:212405
168. Miron IM, Moore T, Szambolics H, Bud Prejbeanu LD, Auffret S, Rodmacq B, Pizzini S, Vogel J, Bonfim M, Schuhl A, Gaudin G (2011) Fast current-induced domain-wall motion controlled by the Rashba effect. Nat Mater 10:419
169. Ohno H, Dietl T (2008) Spin-transfer physics and the model of ferromagnetism in (ga,mn)as. J Magn Magn Mater 320:1293. arXiv:0712.3247
170. Chiba D, Yamanouchi M, Matsukura F, Dietl T, Ohno H (2006) Domain-wall resistance in ferromagnetic (ga,mn)as. Phys Rev Lett 96:096602. arXiv:cond-mat/0601464
171. Thiaville A, Nakatani Y, Miltat J, Suzuki Y (2005) Micromagnetic understanding of current-driven domain wall motion in patterned nanowires. Europhys Lett 69:990
172. Roy PE, Wunderlich J (2011) In-plane magnetic anisotropy dependence of critical current density, walker field and domain-wall velocity in a stripe with perpendicular anisotropy. Appl Phys Lett 99:122504
173. Kurebayashi H, Sinova J, Fang D, Irvine AC, Skinner TD, Wunderlich J, Novak V, Campion RP, Gallagher BL, Vehstedt EK, Zarbo LP, Vyborny K, Ferguson AJ, Jungwirth T (2014) An anti-damping spinorbit torque originating from the berry curvature. Nat Nanotechnol 9:211. arXiv:1306.1893
174. Mizukami S, Ando Y, Miyazaki T (2001) The study on ferromagnetic resonance linewidth for nm/80nife/nm (nm=cu, ta, pd and pt) films. Jpn J Appl Phys 40:580
175. Tserkovnyak Y, Brataas A, Bauer GEW, Halperin BI (2005) Nonlocal magnetization dynamics in ferromagnetic heterostructures. Rev Mod Phys 77:1375. arXiv:cond-mat/0409242

176. Hals KMD, Brataas A, Tserkovnyak Y (2010) Scattering theory of charge-current-induced magnetization dynamics. Euro Phys Lett 90:47002. arXiv:0905.4170
177. Tatara G, Nakabayashi N, Lee KJ (2013) Spin motive force induced by Rashba interaction in the strong sd coupling regime. Phys Rev B 87:054403
178. Ciccarelli C, Hals KMD, Irvine A, Novak V, Tserkovnyak Y, Kurebayashi H, Brataas A, Ferguson A (2014) Magnonic charge pumping via spin orbit coupling. Nat Nanotechnol 10:50–54, 10.1038/nnano.2014.252
179. Núñez AS, Fernández-Rossier J, Abolfath M, MacDonald AH (2004) Optical control of the magnetization damping in ferromagnetic semiconductors. J Magn Magn Mater 272–276:1913
180. Oiwa A, Takechi H, Munekata H (2005) Photoinduced magnetization rotation and precessional motion of magnetization in ferromagnetic (Ga, Mn)As. J Supercond Nov Magn 18:9
181. Wang DM, Ren YH, Liu X, Furdyna JK, Grimsditch M, Merlin R (2007) Light-induced magnetic precession in (Ga,Mn)As slabs: hybrid standing-wave damoneshbach modes. Phys Rev B 75:233308. arXiv:cond-mat/0609646
182. Takechi H, Oiwa A, Nomura K, Kondo T, Munekata H (2007) Light-induced precession of ferromagnetically coupled Mn spins in ferromagnetic (Ga, Mn)As. Phys Status Solidi C 3:4267
183. Qi J, Xu Y, Tolk NH, Liu X, Furdyna JK, Perakis IE (2007) Coherent magnetization precession in GaM-nAs induced by ultrafast optical excitation. Appl Phys Lett 91:112506
184. Qi J, Xu Y, Steigerwald A, Liu X, Furdyna JK, Perakis IE, Tolk NH (2009) Ultrafast laser-induced coherent spin dynamics in ferromagnetic $Ga_{1-x}Mn_xAs$/GaAs structures. Phys Rev B 79:085304
185. Rozkotova E, Nemec P, Horodyska P, Sprinzl D, Trojanek F, Maly P, Novak V, Olejnik K, Cukr M, Jungwirth T (2008) Light-induced magnetization precession in GaMnAs. Appl Phys Lett 92:122507. arXiv:0802.2043
186. Rozkotová E, Němec P, Tesařová N, Malý P, Novák V, Olejník K, Cukr M, Jungwirth T (2008) Coherent control of magnetization precession in ferromagnetic semiconductor (Ga, Mn)As. Appl Phys Lett 93:232505. arXiv:0808.3738
187. Hashimoto Y, Munekata H (2008) Coherent manipulation of magnetization precession in ferromagnetic semiconductor (Ga,Mn)As with successive optical pumping. Appl Phys Lett 93:202506. arXiv:0810.3728
188. Hashimoto Y, Kobayashi S, Munekata H (2008) Photoinduced precession of magnetization in ferromagnetic (Ga, Mn)As. Phys Rev Lett 100:067202
189. Kobayashi S, Suda K, Aoyama J, Nakahara D, Munekata H (2010) Photo-induced precession of magnetization in metal/(Ga, Mn)As systems. IEEE Trans Magn 46:2470
190. Ramsay AJ, Roy PE, Haigh JA, Otxoa RM, Irvine AC, Janda T, Campion RP, Gallagher BL, Wunderlich J (2015) Optical Spin-Transfer-Torque-Driven Domain-Wall Motion in a Ferromagnetic Semiconductor. Phys Rev Lett 114:067202
191. Wang J, Sun C, Hashimoto Y, Kono J, Khodaparast GA, Cywinski L, Sham LJ, Sanders GD, Stanton CJ, Munekata H (2006) Ultrafast magneto-optics in ferromagnetic III-V semiconductors. J Phys Condens Matter 18:R501
192. Kirilyuk A, Kimel AV, Rasing T (2010) Ultrafast optical manipulation of magnetic order. Rev Mod Phys 82:2731
193. Lingos PC, Wang J, Perakis IE (2015) Manipulating femtosecond spin−orbit torques with laser pulse sequences to control magnetic memory states and ringing. Phys Rev B 91:195203. http://arxiv.org/abs/1411.6662.1411.6662